International Journal of Engineering Trends and Technology
ISSN: 2231-5381/ https://doi.org/10.14445/22315381/IJETT-V74I5P127

Volume 74 Issue 5, 411-434, May 2026

Original Article

Effect of Arrhenius Energy and Variable Thermal Conductivity on Blood Flow through the Stenotic Artery

Sumit Kumar[1,2], Surendra Kumar[2]

[1]*Department of Mathematics, Government College for Women, Gurawara (Rewari), Haryana, India*
[2]*University Institute of Engineering and Technology, Maharshi Dayanand University, Rohtak, Haryana, India*

[1]*Corresponding Author : sumit96105@gmail.com*

Received: 24 September 2025 Revised: 10 February 2026 Accepted: 19 February 2026 Published: 30 May 2026

Abstract - *The present research introduces a novel mathematical model that investigates blood flow dynamics in an artery featuring three different types of stenosis, namely irregular, overlapping, and elliptical at the distinct locations, addressing a combination of variable thermal conductivity, Reynolds viscosity model, uniform magnetic field, electrical field, and Arrhenius activation energy effects. After including these concepts in the flow equations, the authors converted them into dimensionless form and finally obtained the numerical solution using the 'Explicit Finite-Difference Method'. This approach finds the graphical representation of velocity with Darcy number, electrokinetic parameter, radiation parameter, Reynolds number, Hartmann number, and the convection volume fraction of the hybrid nanoparticles. The graphical demonstration of temperature with Eckert number, radiation parameter, Prandtl number, and Reynolds number, while the concentration with the activation energy and Schmidt number. The author observed that when the value of the activation energy increases from 2 to 6 then the percentage increment in the concentration profile as 4.71 % increment for the irregular shape of the stenosis, 4.74 % increment for the overlapping shape of the stenosis, and 4.75 % increment for the elliptical shape of the stenosis at the centre of the artery while 12.91 % increment for the irregular shape of the stenosis, 4.39 % increment for the overlapping shape of the stenosis, and 4.31 % increment for the elliptical shape of the stenosis at the 0.5 radius of the artery. The suspension of silver and titanium oxide nanoparticles is incorporated to intensify heat and mass transfer and optimize drug delivery mechanisms with multiple stenoses in a single straight artery. This approach addresses the physiological complexities of multi-stenosed arteries and opens new avenues for targeted therapies and biomedical applications.*

Keywords - *Nanoparticles, Non-Newtonian fluid, Stenosed artery, Variable thermal conductivity, Variable viscosity*.

1. Introduction

Blood is a complicated suspension (mixture) of cells, proteins, lipoproteins, plasma, and ions that help transport nutrients and remove wastes. The flow of Blood in the artery from locations of higher pressure to areas of lower pressure, and the pressure and flow are often unpredictable in general. This phenomenon applies to all types of fluids; therefore, it also happens in blood flow through the arteries or vessels.

The heart continuously beats to send oxygenated and nutrient-rich Blood to all of the body's cells and organs through its complex network of branching muscular elastic arteries. As a result of the cardiac pump's cyclical nature, all arteries pass through the pulsatile condition. In normal conditions, Blood circulates (flows) in a laminar or streamlined pattern with maximum velocity near the centre of the blood vessel when resistance from the vessel walls is negligible. Sankar and Hemalatha [11] conducted a mathematical analysis of the effects of catheterization and non-Newtonian blood properties in arteries. They demonstrated that velocity diminishes when the yield stress increases, but wall shear stress and frictional resistance both enhance.

Gandhi et al. [33] studied the combined impact of hybrid nanoparticles (copper and alumina oxide) and two types of time variant stenosis, specifically trapezoidal and elliptical shapes. Dhange et al. [26] presented a theoretical analysis of the hemodynamic characteristics of blood flow. They are considered the inclined overlapping stenosed arterial with the Casson model of fluid. Tripathi and Sharma [9] investigated mass transfer and heat transfer in the symmetrical shape of the stenosis.

This study reveals the impact of radiation effect and the compression of streamlines of the arterial blockage in three different conditions. Yadav and Singh [30] discussed a comparative biomedical simulation model with the irregular and overlapping stenosis at the same location. They concluded the final observation after employing the concepts of

hematocrit viscosity (variable viscosity), non-Newtonian Sutterby rheological fluid, electroosmosis, and hybrid nanofluid ($Ag - TiO_2$/Blood). Islam et al. [37] presented a mathematical model of the electroosmosis force using the non-Newtonian Sutterby fluid model in the ternary hybrid nanofluid ($TiO_2 - SiO_2 - Al_2O_3$/Blood). They observed that the enhancement of the motion of the ternary blood nanofluid ($TiO_2 - SiO_2 - Al_2O_3$/Blood) Due to the electroosmotic variable. Akbar [29] explores the biomathematical analysis of the three types of arteries using the Sutterby fluid model. Souai et al. [40] investigated the combined impact of mass transfer and transfer in a hybrid nanofluid with an n-shape porous medium. They address the concept of MHD-DDMC (magnetohydrodynamic double-diffusive mixed convection) and use the global sensitivity analysis and lattice Boltzmann method in their research. Zar et al. [31] address the behavior of blood flow in the inclined stenotic arteries with copper and graphene nanoparticles using the 'Akbari Ganji Method' (AGM) and the 'Homotopy Perturbation Method' (HPM). Their findings indicate that the minimal error for the temperature and axial velocity is 8.8×10^{-10} and $2.34\times10^{-10,}$ respectively. Bagherkhani et al. [24] explore the effect of magnetic and electric fields in the irregular multi-stenosed artery associated with gold nanoparticles and iron oxide nanoparticles. Aktar et al. [1] provided a theoretical analysis of pulsatile blood flow with the presence of gold nanoparticles in Blood and two types of abnormality in the bifurcated artery, namely aneurysm and stenosis.

Their finding reveals that the nanoparticle volume fraction, magnetic field, Reynolds number, and power law index exert a significant influence on the isotherms, Wall Shear Stress (WSS), heat transfer coefficient, and velocity in pulsatile blood flow with the presence of the aneurysm and stenosis in the bifurcated artery.

Abdelsalam and Bhatti [36] investigated blood flow dynamics in stenosed arteries by incorporating gold and silver nanoparticles under Electromagnetohydrodynamic (EMHD) effects. Their study revealed that thermal induction leads to a slight arterial wall expansion, which in turn enlarges the cross-sectional area of the stenotic zone. This expansion reduces the degree of narrowing and lowers flow resistance.

The results provide valuable insights into the hemodynamic behavior of blood flow within stenosed arteries in the presence of hybrid gold and copper nanoparticles. Sangapatnam [39] investigated blood flow with the Casson fluid when the cosine shape of the stenosis is present in an artery near the arterial wall. Zuberi et al. [14] focused on numerical simulation of blood flow in the artery, considering the thermal radiation, magnetic fields and key flow parameters.

In this study, a two-dimensional Newtonian model is used and findings highlight the role of nanoparticles in enhancing therapeutic strategies for stenosis and advancing biomedical applications. Thirunananasambantham et al. [22] presented a computational analysis of hybrid generalized power low blood flow with a cosine-shaped occlusion in the straight stenosed artery. They used COMSOL Multiphysics software for graphical representation and analysis of the effect of silver nanoparticles, gold nanoparticles, hybrid nanoparticles, external magnetic field, and percentage occlusion of the cosine-shaped stenosis. Turabi et al. [43] studied the Magnetohydrodynamic (MHD) effect and predicted thermal enhancement mechanisms using the Finite Element Method (FEM) in the blood flow via an inflamed artery. Dhange et al. [25] reviewed the hemodynamic properties of blood flow and investigated the nonlinear behavior of Blood with the overlapping stenosis in the artery.

The primary focus is on gold nanoparticle suspension, inclined angle, and force field. Hira et al. [12] explore the Arterial Neural Network (ANNs) for advanced computational modeling in a stenosed artery with the combined effects of Darcy Forchheimer, copper nanoparticle, titanium oxide nanoparticle, and hybrid nanoparticles. Suneetha and Ramasekhar [41] studied the Casson Fluid (Blood) flow associated with stenosis near the inner arterial wall. Salahuddin et al. [42] work explores chemical reaction and heat generation effects in micropolar fluid flowing. They are employing the Low Reynolds Number (LRN) and long Wavelength (LWL) conditions for reducing the complexity of the governing flow equations. Asha and Srivastava [21] analysed the combined effects of various shapes (namely sphere, brick, cylinder, platelet, blade, laminar) of hybrid nanoparticles, curved artery with axisymmetric constriction, heat absorption parameter, slip parameter, and Grashof number.

Hussian et al. [4] explore a detailed three-dimensional analysis of steady and pulsatile blood flow in a stenosed artery with both Newtonian and experimentally characterized viscoelastic PTT blood models. Chauhan and Sasmal [2] research characterizes the flow of Blood in a vessel which has a stenosis followed by a post-stenotic dilatation, by modelling the Blood as a non-Newtonian Sisko fluid and then solving the governing equations using the use of finite element method.

It is found that parametric analysis shows that the severity of stenosis, the degree of dilatation, and the Sisko model parameters are significant determinants of velocity, pressure, shear stress, and temperature that give a deeper insight into the hemodynamics associated with the progression of atherosclerotic disease and clinical implications. Haider et al. [16] analyzed blood flow in elliptically shaped arteries with several stenotic lesions in terms of the Carreau non-Newtonian fluid model in combination with Navier-Stokes equations, which are resolved using Finite Element and Finite Volume Methods.

The findings reveal that the size, shape, and location of stenosis have a significant impact on velocity, distribution of pressure, temperature, and flow perturbation, which could be instrumental in disease progression, treatment planning, and design of the vascular device. Hussain et al. [3] investigate blood flow and heat transfer in a trapezoidally stenosed artery based on the non-Newtonian Sisko model to obtain the joint effects of complicated geometry and rheological behavior. Numerical findings demonstrate that the severity of stenosis is a strong determinant of velocity, pressure, temperature, shear stress, and flow resistance, which is a novel discovery of the hemodynamic and thermal processes of vascular pathologies.

The study by Parida et al. [10] is an unsteady computational investigation of blood flow in a time-dependent multi-stenosed artery utilizing a viscoelastic Jeffrey fluid with Caputo-Fabrizio fractional derivatives, applying magnetic, thermal, chemical, and body-force forces and a ternary hybrid nanofluid ($Au - Ag - MWCNT$). Semi-analytical solutions with ANN-based prediction show important improvements in heat and mass transfer, and provide clarity on the use of fractional order, magnetic field, and flow parameters with applications in hyperthermia and in the delivery of specific drugs.

Zeeshan et al. [7] numerically examined the case of unsteady pulsatile blood flow and heat transfer within a vertical stenosed artery with the model of Blood as a Bingham fluid under a magnetic field by applying the explicit finite difference method. The findings indicate that higher Bingham and thermal parameters improve flow and wall shear stress and that higher magnetic fields repress velocity and raise impedance with implications on cardiovascular therapy and biomedical device design.

Singh and Yadav [6] analytically measure the electro-magnetohydrodynamic blood flow in a tapered, curved, and overlapped stenosed artery with $Ag - GO - ZrO_2$ /blood ternary hybrid nanofluid under axial electric, magnetic, and azimuthal magnetic fields.

The findings indicate an improvement in velocity with the nanoparticle loading, the increase in the wall shear stress and pressure gradient in divergent arteries, and the high prediction accuracy of the ANN, which demonstrates the use of the model in the delivery of targeted drugs and the treatment of arterial diseases. Shah et al. [27] examined the magneto-thermal blood flow over a stenotic artery and time-fractional Sutterby fluid modeling of Blood based on non-Newtonian and memory effects.

The results of numerical solutions using the finite difference technique indicate that the strength of the magnetic field, the order of the fraction, and thermal radiation play a significant role in determining the velocity and temperature distributions, which can serve as a base in future machine-learning-assisted prediction of the complex hemodynamic flows.

1.1. Research gap

Several studies have analysed blood flow in arteries with shaped or differently shaped stenoses, without nanoparticle additions and with nanoparticle additions improving heat transfer and flow stability [30, 35, 40]. However, the existing research addressing multiple stenoses, each with different geometric profiles and spatial locations in a single straight or curved artery, remains limited. Existing models have explored bell, elliptical, triangular, rectangular, cosine, and sine-shaped stenoses, but researchers generally focus on isolated cases and do not fully capture the complex interactions of sequential obstructions.

Recent advances in hybrid nanoparticle suspensions, those involving silver and titanium oxide, have demonstrated enhanced thermal and electrical conductivity as well as improved biocompatibility and blood compatibility. The silver nanoparticles offer notable antimicrobial and anti-inflammatory characteristics, reducing wall shear stress and assisting in targeted drug delivery. The titanium oxide nanoparticles display strong cardiovascular therapeutic effects and efficient heat transfer properties, with promising results for enhancing medication clustering and reducing viscosity.

1.2. Novelty contributions

The present research introduces a novel mathematical model that investigates blood flow dynamics in an artery featuring three different types of stenosis, namely irregular, overlapping, and elliptical at the distinct locations, addressing a combination of variable thermal conductivity, Reynolds viscosity model, uniform magnetic field, electrical field, and Arrhenius activation energy effects. The suspension of silver and titanium oxide nanoparticles is incorporated to intensify heat and mass transfer and optimize drug delivery mechanisms with multiple stenoses in a single straight artery. This approach addresses the physiological complexities of multi-stenosed arteries and opens new avenues for targeted therapies and biomedical applications.

2. Formulation of the Problem

In a cylindrical coordinate system, as $(\tilde{r}, \tilde{\theta}, \tilde{z})$ and $\tilde{z}$ represents the flow direction of the Blood, but it is actually the axial coordinate. The $\tilde{\theta}$ represents the circumferential coordinate in the artery, and due to the axis-symmetric flow of the Blood in the artery, it is eliminated in the current mathematical model. Finally, $\tilde{r}$ denoted the radial coordinate in this model. Now, authors explain the three different types of stenosis (irregular, overlapping, and elliptical) at the three distinct locations in the single straight artery. The geometry of the artery is represented mathematically using the cylindrical coordinates in Equation (1) and a graphical representation in Figure 1.

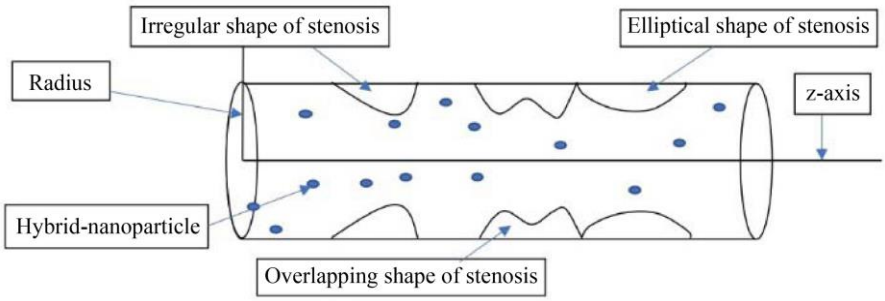

Fig. 1 Geometry of the artery

2.1. Geometry of the problem

This model consists of three types of stenotic segments at the three distinct locations. The first one is the irregular shape of the stenosis, which is located between $\tilde{z}_s$ to $\tilde{z}_s + \tilde{z}_l$Second is the overlapping shape of the stenosis, which is located between $\tilde{z}_s + 2\tilde{z}_l$ to $\tilde{z}_s + 3\,\tilde{z}_l$ and third is the elliptical shape of the stenosis, which is located between $\tilde{z}_s + 3\,\tilde{z}_l$ to $\tilde{z}_s + 4\,\tilde{z}_l$. There are some researchers (Yadav and Singh [30], Gandhi et al. [33]) who have used the elliptical shape of the stenosis in their research works. Further, move the overlapping shape. This shape is the main focus for research by the following researchers: Dhange et al. [25], Yadav and Singh [30]. Finally, the authors noted the irregular shape of the stenosis used by Yadav and Singh [30] in their research area. The mathematical representation of these three stenoses in $(\tilde{r}, \tilde{\theta}, \tilde{z})$ The coordinate is as follows:

$$\tilde{R}(\tilde{z}) = \begin{cases} \tilde{R}_0 - \frac{\tilde{\delta}}{\tilde{z}_l^h}\left(\frac{h^{h/(h-1)}}{h-1}\right) H_1\,; & \tilde{z}_s \le \tilde{z} \le \tilde{z}_s + \tilde{z}_l \\ \tilde{R}_0 - \frac{3\tilde{\delta}}{8} H_2 & ;\ \ \tilde{z}_s + 2\tilde{z}_l \le \tilde{z} \le \tilde{z}_s + 3\tilde{z}_l \\ \tilde{R}_0 - \tilde{\delta}\, H_3 & ;\ \ \tilde{z}_s + 3\tilde{z}_l \le \tilde{z} \le \tilde{z}_s + 4\tilde{z}_l \\ \tilde{R}_0 & ; \qquad otherwise \end{cases} \tag{1}$$

where, $\tilde{\xi}_e = \tilde{z} - \tilde{z}_s - 2\tilde{z}_l$, $H_3 = sin\left[\frac{\pi(\tilde{z}-\tilde{z}_s-3\tilde{z}_l)}{\tilde{z}_l}\right]$

$H_1 = \left[\tilde{z}_l^{h-1}(\tilde{z} - \tilde{z}_s) - (\tilde{z} - \tilde{z}_s)^h\right]$

$H_2 = \frac{11}{\tilde{z}_l}\left(\tilde{\xi}_e\right) - \frac{47}{\tilde{z}_l^2}\left(\tilde{\xi}_e\right)^2 + \frac{72}{\tilde{z}_l^3}\tilde{\xi}_e{}^3 - \frac{36}{\tilde{z}_l^4}\left(\tilde{\xi}_e\right)^4$

In the aforementioned equation, $\tilde{R}_0$ −stands for non-stenotic segment, $\tilde{R}(\tilde{z})$ −stands for stenotic segment, $\tilde{\delta}$ −stands for the maximum height (depth) of the stenosis, $\tilde{z}_s$ denotes the starting point of the overlapping stenotic segment in the artery, $\tilde{z}_l$ is denotes the length of the stenotic regions for all shapes (irregular, overlapping, and elliptical).

2.2. Model Assumptions

These are the assumptions that are made by the hybrid nanofluid blood flow model that is currently proposed:

- A single-phase electrolyte solution is formed by the Blood, which is a mixture of nanoparticles of Ag and TiO_2.
- For the purposes of the realistic scenarios, it is presumed that the Reynolds viscosity model is the one that represents the viscosity of the fluid (Blood).
- In accordance with the presumption of a low magnetic Reynolds number, the induced magnetic field is neglected in comparison to the magnetic field that is applied.
- At low Reynolds numbers (Re), Blood is shown to be laminar, with viscous effects being more prominent than inertial effects that are present.
- The morphology of nanoparticles is cylindrical, as their name suggests, in the current model.
- A uniform magnetic field is applied in the radial direction or perpendicular to the flow direction.
- An electric field is applied in the direction of the flow.

2.3. Governing Flow Equations

Many researchers focus on the Sutterby fluid in the field of blood flow through the artery, but some researchers, such as Islam et al. [37], work on the Sutterby fluid with electroosmotic flow using the ternary hybrid nanoparticles; Akbar [29] and Hussain [38]. The viscosity of Blood is considered from the Reynolds viscosity model to reflect conditions that are realistic, and this model is employed by the researchers (Ellahi et al. [32], Gandhi et al. [34]).

It is shown that as Blood flows through the stenosed artery, it experiences energy loss owing to internal friction, with the lost mechanical energy being transformed into heat within the fluid (Blood), a phenomenon known as viscous dissipation (Barker et al. [5]). (Sharma and Gandhi [8], Glili et al. [15], Manchi and Ponalagusamy [35]).

The velocity, concentration, and temperature fields are as follows (Sharma and Gandhi [8], Glili et al. [15], Tripathi et al. [17], Tripathi et al. [19], Manchi and Ponalagusamy [35]):

$$\tilde{V} = \left[\tilde{u}(\tilde{r}, \tilde{\theta}, \tilde{z}, \tilde{t}), \tilde{v}(\tilde{r}, \tilde{\theta}, \tilde{z}, \tilde{t}), \tilde{w}(\tilde{r}, \tilde{\theta}, \tilde{z}, \tilde{t})\right],$$
$$\tilde{C} = \tilde{C}(\tilde{r}, \tilde{\theta}, \tilde{z}, \tilde{t}),\ \ \tilde{T} = \tilde{T}(\tilde{r}, \tilde{\theta}, \tilde{z}, \tilde{t})$$

The governing equations for continuity, momentum (using the concept of body acceleration, porous media, electroosmosis, Lorentz forces, buoyancy effect), energy (uniform magnetic field, radiation effect, and viscous

dissipation), and concentration (Arrhenius activation energy) incorporating with hybrid nanofluid in the given system of coordinates are as follows (Glili et al. [15], Yadav and Singh [30], Gandhi et al. [34])

$$\frac{\partial \tilde{u}}{\partial \tilde{r}} + \frac{\tilde{u}}{\tilde{r}} + \frac{\partial \tilde{w}}{\partial \tilde{z}} = 0 \tag{2}$$

$$\rho_{hnf}\left(\frac{\partial \tilde{u}}{\partial \tilde{t}} + \tilde{u}\frac{\partial \tilde{u}}{\partial \tilde{r}} + \tilde{w}\frac{\partial \tilde{u}}{\partial \tilde{z}}\right) = -\frac{\partial \tilde{p}}{\partial \tilde{r}} + \left(\frac{\partial}{\partial \tilde{z}}(S_{\tilde{r}\tilde{z}}) + \frac{1}{\tilde{r}}\frac{\partial}{\partial \tilde{r}}(S_{\tilde{r}\tilde{r}})\right) - \mu_{hnf}\frac{\tilde{u}}{\tilde{r}^2} \tag{3}$$

$$\rho_{hnf}\left(\frac{\partial \tilde{w}}{\partial \tilde{t}} + \tilde{u}\frac{\partial \tilde{w}}{\partial \tilde{r}} + \tilde{w}\frac{\partial \tilde{w}}{\partial \tilde{z}}\right) = -\frac{\partial \tilde{p}}{\partial \tilde{z}} - \frac{\mu_{hnf}}{k_p}\tilde{w} + \rho_e E_{\tilde{z}} - \sigma_{hnf}B_0^2\tilde{w} + \left(\frac{\partial}{\partial \tilde{z}}(S_{\tilde{z}\tilde{z}}) + \frac{1}{\tilde{r}}\frac{\partial}{\partial \tilde{r}}(S_{\tilde{r}\tilde{z}})\right) + g(\gamma\rho)_{hnf}(\tilde{T} - \tilde{T}_0) + g(\gamma\rho)_{hnf}(\tilde{C} - \tilde{C}_0) + \rho_{hnf}G(\tilde{t}) \tag{4}$$

$$(\rho C_p)_{hnf}\left(\frac{\partial \tilde{T}}{\partial \tilde{t}} + \tilde{u}\frac{\partial \tilde{T}}{\partial \tilde{r}} + \tilde{w}\frac{\partial \tilde{T}}{\partial \tilde{z}}\right) = \frac{1}{\tilde{r}}\frac{\partial}{\partial \tilde{r}}\left(k(\tilde{T})\tilde{r}\frac{\partial \tilde{T}}{\partial \tilde{r}}\right) + \frac{\partial}{\partial \tilde{z}}\left(k(\tilde{T})\frac{\partial \tilde{T}}{\partial \tilde{z}}\right) - \frac{\partial \tilde{q}_{\tilde{r}}}{\partial \tilde{r}} + \sigma_{hnf}B_0^2\tilde{w}^2 + \mu_{hnf}\left[\left(\frac{\partial \tilde{u}}{\partial \tilde{r}}\right)^2 + \left(\frac{\tilde{u}}{\tilde{r}}\right)^2 + \left(\frac{\partial \tilde{w}}{\partial \tilde{z}}\right)^2 + \frac{1}{2}\left(\frac{\partial \tilde{u}}{\partial \tilde{z}} + \frac{\partial \tilde{w}}{\partial \tilde{r}}\right)^2\right] \tag{5}$$

$$\left(\frac{\partial \tilde{C}}{\partial \tilde{t}} + \tilde{u}\frac{\partial \tilde{C}}{\partial \tilde{r}} + \tilde{w}\frac{\partial \tilde{C}}{\partial \tilde{z}}\right) = D_m\left(\frac{\partial^2 \tilde{C}}{\partial \tilde{r}^2} + \frac{1}{\tilde{r}}\frac{\partial \tilde{C}}{\partial \tilde{r}} + \frac{\partial^2 \tilde{C}}{\partial \tilde{z}^2}\right) - \tilde{k}_{\tilde{r}}^2\left(\frac{\tilde{T}}{\tilde{T}_0}\right)^q exp\left[-\frac{E_b}{k_0\tilde{T}}\right](\tilde{C} - \tilde{C}_0) \tag{6}$$

where, $\tilde{C}(\tilde{r},\tilde{z},\tilde{t})$, $\tilde{u}(\tilde{r},\tilde{z},\tilde{t})$, $\tilde{T}(\tilde{r},\tilde{z},\tilde{t})$ $\tilde{w}(\tilde{r},\tilde{z},\tilde{t})$, are the concentration, radial velocity, temperature, and axial velocity profiles, respectively. In the above governing equations, the extra stress tensor components are given as

$$S_{\tilde{r}\tilde{r}} = \mu_{hnf}\left[1 - \frac{mB^2}{6}\left(\frac{\partial \tilde{u}}{\partial \tilde{z}} + \frac{\partial \tilde{w}}{\partial \tilde{r}}\right)^2\right]2\frac{\partial \tilde{u}}{\partial \tilde{r}} - \left[\mu_{hnf}\frac{mB^2}{3}\left\{2\left(\left(\frac{\partial \tilde{u}}{\partial \tilde{r}}\right)^2 + \left(\frac{\tilde{u}}{\tilde{r}}\right)^2 + \left(\frac{\partial \tilde{w}}{\partial \tilde{z}}\right)^2\right)\right\}\right]\frac{\partial \tilde{u}}{\partial \tilde{r}} \tag{7}$$

$$S_{\tilde{r}\tilde{z}} = \mu_{hnf}\left[1 - \frac{mB^2}{6}\left(\frac{\partial \tilde{u}}{\partial \tilde{z}} + \frac{\partial \tilde{w}}{\partial \tilde{r}}\right)^2\right]\left[\frac{\partial \tilde{w}}{\partial \tilde{r}} + \frac{\partial \tilde{u}}{\partial \tilde{z}}\right] - \left[\mu_{hnf}\frac{mB^2}{6}\left\{2\left(\left(\frac{\partial \tilde{u}}{\partial \tilde{r}}\right)^2 + \left(\frac{\tilde{u}}{\tilde{r}}\right)^2 + \left(\frac{\partial \tilde{w}}{\partial \tilde{z}}\right)^2\right)\right\}\right]\left[\frac{\partial \tilde{w}}{\partial \tilde{r}} + \frac{\partial \tilde{u}}{\partial \tilde{z}}\right] \tag{8}$$

$$S_{\tilde{z}\tilde{z}} = \mu_{hnf}\left[1 - \frac{mB^2}{6}\left(\frac{\partial \tilde{u}}{\partial \tilde{z}} + \frac{\partial \tilde{w}}{\partial \tilde{r}}\right)^2\right]\left[2\frac{\partial \tilde{w}}{\partial \tilde{z}}\right] - \left[\mu_{hnf}\frac{mB^2}{6}\left\{2\left(\left(\frac{\partial \tilde{u}}{\partial \tilde{r}}\right)^2 + \left(\frac{\tilde{u}}{\tilde{r}}\right)^2 + \left(\frac{\partial \tilde{w}}{\partial \tilde{z}}\right)^2\right)\right\}\right]\left[2\frac{\partial \tilde{w}}{\partial \tilde{z}}\right] \tag{9}$$

Here, physical parameters that emerge in the above Equations (6) to (10) are as follows: ρ_{hnf} −stands for the density of the hybrid nanofluid, μ_{hnf} −stands for the viscosity of the hybrid nanofluid, $S_{\tilde{r}\tilde{r}}$ −stands for normal stress in the radial direction, $S_{\tilde{r}\tilde{z}}$ −stands for the shear stress action in $\tilde{z}$ direction on a plane normal to $\tilde{r}$, $S_{\tilde{z}\tilde{z}}$ −stands for the in the axial direction, $\tilde{p}$ −stands for pressure, $\tilde{t}$ −stands for time, ρ_e −stands for electrical charge density, $E_{\tilde{z}}$ −applied electric field in $\tilde{z}$ direction, σ_{hnf} −stands for the electrical conductivity of the hybrid nanofluid, B_0 −stands for the applied magnetic field strength, g −stands gravitational acceleration, γ_{hnf} −stands for the thermal expansion coefficient, k_p −stands for the permeability of a porous medium, $(C_p)_{hnf}$ −stands for the specific heat capacity of the hybrid nanofluid, $\tilde{q}_{\tilde{r}}$ −stands for radiative heat flux, $k(\tilde{T}) = k_{hnf}\left(1 + \alpha_1((\tilde{T} - \tilde{T}_0)/(\tilde{T}_w - \tilde{T}_0))\right)$ −stands for variable thermal conductivity of hybrid nanofluid ($\tilde{T}_0$ is the reference temperature and $\tilde{T}_w$ is the temperature at the wall), D_m −stands for mass diffusivity, E_n −stands for the activation energy, $k_{\tilde{r}}$ −stands for the rate of the chemical reaction, k_0 −stands for the constant of Boltzmann, term $\tilde{k}_{\tilde{r}}^2\left(\frac{\tilde{T}}{\tilde{T}_0}\right)^q exp\left[-\frac{E_n}{k_0\tilde{T}}\right]$ stands for the equation of revised Arrhenius, term $\sigma_{hnf}B_0^2\tilde{w}^2$ stands for Joule heating due to MHD effect, term $\mu_{hnf}\left[\left(\frac{\partial \tilde{u}}{\partial \tilde{r}}\right)^2 + \left(\frac{\tilde{u}}{\tilde{r}}\right)^2 + \left(\frac{\partial \tilde{w}}{\partial \tilde{z}}\right)^2 + \frac{1}{2}\left(\frac{\partial \tilde{u}}{\partial \tilde{z}} + \frac{\partial \tilde{w}}{\partial \tilde{r}}\right)^2\right]$ stands for the viscous dissipation conversion of kinetic energy to heat due to fluid viscosity, term $\rho_e E_{\tilde{z}}$ stand electroosmotic body force per unit volume (ρ_e is the net electrical charge density within the fluid. It arises from the imbalance of cations and anions in the EDL region adjacent to vessel walls or surfaces. In a physiological or nanofluid context. It is derived from the Boltzmann distribution and related to ion concentrations at equilibrium. $\rho_e = z_0 e_0(n_+ - n_-)$, where z_0 is the ionic balance, e_0 is the electrical charge, n_+ is cation density, n_- is the anion density), term $G(\tilde{t}) = a_g\left(cos(w_p\tilde{t} + \alpha)\right)$ stands for body acceleration (a_g is the amplitude of the body acceleration. This is the maximum acceleration imparted to fluid at any point in the cycle, $w_p = 2\pi f_b$ is the angular frequency which determines how fast the oscillations occur and f_b is the body force frequency, which reflects the rate of periodic acceleration, α is the phase angle, and $\tilde{t}$ is the time), term $-\frac{\partial \tilde{p}}{\partial \tilde{z}} = A_0 + A_1 cos(2\pi f_p\tilde{t})$ stands for the axial pressure gradient (A_0 is the constant (steady) component of the pressure gradient, representing the average driving force for the flow. A_1 is the amplitude of the oscillatory (pulsatile) component, dictating how much the pressure gradient fluctuates around its mean value, this $cos(2\pi f_p\tilde{t})$ The term introduces periodicity with the frequency. f_p).

2.4. Viscosity Model and Thermophysical Parameter

The Reynolds viscosity model (temperature-dependent viscosity) and the thermophysical parameters are crucial for accurately describing the flow of Blood (based on a hybrid nanofluid) (Sharma and Gandhi [8], Glili et al. [15], Tripathi et al. [17], Tripathi et al. [19], Manchi and Ponalagusamy [35]).

$\mu_f(\tilde{T}) = \mu_0 e^{-\beta_0((\tilde{T}-\tilde{T}_0)/(\tilde{T}_w-\tilde{T}_0))}$ here, $\beta_0 \ll 1$.

Viscosity for nanofluid (silver and titanium oxide) and hybrid nanofluid with composition of silver, titanium, and Blood, incorporating the following ways:

Silver
$\mu_{nf} = \frac{\mu_f(\tilde{T})}{(1-\phi_{Ag})^{2.5}}$,
titanium oxide
$\mu_{nf} = \frac{\mu_f(\tilde{T})}{(1-\phi_{TiO_2})^{2.5}}$,
Hybrid nanofluid
$\mu_{hnf} = \frac{\mu_f(\tilde{T})}{(1-\phi_{Ag})^{2.5}(1-\phi_{TiO_2})^{2.5}}$

Density for nanofluid (silver and titanium oxide) and hybrid nanofluid with composition of silver, titanium, and Blood, incorporating the following ways:

Silver
$\rho_{nf} = (1-\phi_{Ag})\rho_f + \phi_{Ag}\rho_{Ag}$,
Titanium oxide
$\rho_{nf} = (1-\phi_{TiO_2})\rho_f + \phi_{TiO_2}\rho_{TiO_2}$,
Hybrid nanofluid
$\rho_{hnf} = (1-\phi_{TiO_2})[(1-\phi_{Ag})\rho_f + \phi_{Ag}\rho_{Ag}] + \phi_{TiO_2}\rho_{TiO_2}$

Heat capacity for nanofluid (silver and titanium oxide) and hybrid nanofluid with composition of silver, titanium, and Blood, incorporating the following ways:

Silver
$(\rho c_p)_{nf} = (1-\phi_{Cu})(\rho c_p)_f + \phi_{Cu}(\rho c_p)_{Cu}$,
Titanium oxide
$(\rho c_p)_{nf} = (1-\phi_{Cu})(\rho c_p)_f + \phi_{Cu}(\rho c_p)_{Cu}$,
Hybrid nanofluid
$(\rho c_p)_{hnf} = (1-\phi_{Al_2O_3})\left[(1-\phi_{Cu})(\rho c_p)_f + \phi_{Cu}(\rho c_p)_{Cu}\right] + \phi_{Al_2O_3}(\rho c_p)_{Al_2O_3}$

Thermal expansion coefficient for nanofluid (silver and titanium oxide) and hybrid nanofluid with composition of silver, titanium, and Blood, incorporating the following ways:

Silver
$\frac{(\rho\gamma)_{nf}}{(\rho\gamma)_f} = (1-\phi_{Ag}) + \phi_{Ag}\frac{(\rho\gamma)_{Ag}}{(\rho\gamma)_f}$,
Titanium oxide
$\frac{(\rho\gamma)_{nf}}{(\rho\gamma)_f} = (1-\phi_{TiO_2}) + \phi_{TiO_2}\frac{(\rho\gamma)_{TiO_2}}{(\rho\gamma)_f}$,
Hybrid nanofluid
$\frac{(\rho\gamma)_{hnf}}{(\rho\gamma)_f} = (1-\phi_{TiO_2})\left[(1-\phi_{Ag}) + \phi_{Ag}\frac{(\rho\gamma)_{Cu}}{(\rho\gamma)_f}\right] + \phi_{TiO_2}\frac{(\rho\gamma)_{TiO_2}}{(\rho\gamma)_f}$

Thermal conductivity for nanofluid (silver and titanium oxide) and hybrid nanofluid with composition of silver, titanium, and Blood, incorporating the following ways:

Silver
$\frac{\kappa_{nf}}{\kappa_f} = \frac{\kappa_{Ag}+2\kappa_f-2\phi_{Ag}(\kappa_f-\kappa_{Ag})}{\kappa_{Ag}+2\kappa_f+\phi_{Ag}(\kappa_f-\kappa_{Ag})}$,
Titanium oxide
$\frac{\kappa_{nf}}{\kappa_f} = \frac{\kappa_{TiO_2}+2\kappa_f-2\phi_{TiO_2}(\kappa_f-\kappa_{TiO_2})}{\kappa_{TiO_2}+2\kappa_f+\phi_{TiO_2}(\kappa_f-\kappa_{TiO_2})}$,
Hybrid nanofluid
$\frac{\kappa_{hnf}}{\kappa_f} = \left[\frac{\kappa_{TiO_2}+2\kappa_{nf}-2\phi_{TiO_2}(\kappa_{nf}-\kappa_{TiO_2})}{\kappa_{TiO_2}+2\kappa_{nf}+\phi_{TiO_2}(\kappa_{nf}-\kappa_{TiO_2})}\right]\left[\frac{\kappa_{Ag}+2\kappa_f-2\phi_{Ag}(\kappa_f-\kappa_{Ag})}{\kappa_{Ag}+2\kappa_f+\phi_{Ag}(\kappa_f-\kappa_{Ag})}\right]$

Electrical conductivity for nanofluid (silver and titanium oxide) and hybrid nanofluid with composition of silver, titanium, and Blood, incorporating the following ways:

Silver
$\frac{\sigma_{nf}}{\sigma_f} = \frac{\sigma_{Ag}+3.9\sigma_f-3.9\phi_{Ag}(\sigma_f-\sigma_{Ag})}{\sigma_{Ag}+3.9\sigma_f+\phi_{Ag}(\sigma_f-\sigma_{Ag})}$,

Titanium oxide
$\frac{\sigma_{nf}}{\sigma_f} = \frac{\sigma_{TiO_2}+3.9\sigma_f-3.9\phi_{TiO_2}(\sigma_f-\sigma_{TiO_2})}{\sigma_{TiO_2}+3.9\sigma_f+\phi_{TiO_2}(\sigma_f-\sigma_{TiO_2})}$,

Hybrid nanofluid
$\frac{\sigma_{hnf}}{\sigma_f} = \left[\frac{\sigma_{TiO_2}+3.9\sigma_{nf}-3.9\phi_{TiO_2}(\sigma_{nf}-\sigma_{TiO_2})}{\sigma_{TiO_2}+3.9\sigma_{nf}+\phi_{TiO_2}(\sigma_{nf}-\sigma_{TiO_2})}\right]\left[\frac{\sigma_{Ag}+3.9\sigma_f-3.9\phi_{Ag}(\sigma_f-\sigma_{Ag})}{\sigma_{Ag}+3.9\sigma_f+\phi_{Ag}(\sigma_f-\sigma_{Ag})}\right]$

Table1. Thermophysical properties of silver, titanium oxide nanofluid, and Blood, their values.

Properties [23]	Blood	Silver	Alumina Oxide
Density	1063	10500	4250
Heat Capacity	3594	235	686.2
Thermal Expansion Coefficient ($\boldsymbol{\gamma \times 10^{-5}}$)	0.18	1.89	0.9
Thermal Conductivity	0.492	429	8.9538
Electrical Conductivity	6.67×10^{-1}	6.3×10^{7}	2.38×10^{6}

2.4.1. Initial and Boundary Conditions

The initial and Boundary conditions are essential to solve the governing (blood flow) equations, as the system state at the start and at physical boundaries.

Initial conditions

The initial conditions define the hybrid nanofluid's velocity, temperature, and concentration at the time. $\tilde{t} = 0$ as $\tilde{w}(\tilde{r},\tilde{t}) = 0,\ \tilde{T}(\tilde{r},\tilde{t}) = 0, \tilde{C}(\tilde{r},\tilde{t}) = 0$ at $\tilde{t} = 0$

Boundary conditions

The boundary conditions determine how the fluid interacts with the wall of the artery, and the symmetry of the artery planes:

$\tilde{w}(\tilde{r},\tilde{t}) = 0$ at $\tilde{r} = \tilde{R}(\tilde{z})$.
$\tilde{T}(\tilde{r},\tilde{t}) = \tilde{T}_w, \tilde{C}(\tilde{r},\tilde{t}) = \tilde{C}_w$ at $\tilde{r} = \tilde{R}(\tilde{z})$

Due to the symmetry axis, velocity, temperature, and concentration at $\tilde{r} = 0$ are $\frac{\partial \tilde{w}(\tilde{r},\tilde{t})}{\partial \tilde{r}} = 0$,
$\frac{\partial \tilde{T}(\tilde{r},\tilde{t})}{\partial \tilde{r}} = 0, \frac{\partial \tilde{C}(\tilde{r},\tilde{t})}{\partial \tilde{r}} = 0.$

2.5. Non-Dimensionalization

The non-dimensional variables and dimensional analysis are crucial for the hybrid nanofluid model. Now, transform the Equations (1) to (10) using physical reference scales into dimensionless form governed by dimensionless numbers, allowing general insightful study of Blood, heat and mass transfer and enabling comparative predictions for various fluids and geometries (Sharma and Gandhi [8], Glili et al. [15], Tripathi et al. [17], Tripathi et al. [19], Coronel et al. [23], Ahammad and Talea [28], Yadav and Singh [30], Manchi and Ponalagusamy [35]).

$$r = \frac{\tilde{r}}{\tilde{R}_0},\quad w = \frac{\tilde{w}}{\tilde{u}_e},\ u = \frac{\tilde{z}_l \tilde{u}}{\tilde{u}_e \tilde{\delta}},\ z = \frac{\tilde{z}}{\tilde{z}_l},\ R(z) = \frac{\tilde{R}(\tilde{z})}{\tilde{R}_0},\quad p = \frac{\tilde{R}_0^2\, \tilde{p}}{\tilde{u}_e\, \tilde{z}_l \mu_0},\ t = \frac{\tilde{u}_e\, \tilde{t}}{\tilde{R}_0},\ d = \frac{\tilde{z}_s}{\tilde{z}_l},\ \theta = \frac{\tilde{T}-\tilde{T}_0}{\tilde{T}_w-\tilde{T}_0},\ \phi = \frac{\tilde{C}-\tilde{C}_0}{\tilde{C}_w-\tilde{C}_0},\ S_{rr} = \frac{\tilde{z}_l\, S_{\tilde{r}\tilde{r}}}{\tilde{u}_e \mu_0},\quad S_{rz} = \frac{\tilde{R}_0\, S_{\tilde{r}\tilde{z}}}{\tilde{u}_e \mu_0},\quad S_{zz} = \frac{\tilde{z}_l\, S_{\tilde{z}\tilde{z}}}{\tilde{u}_e \mu_0},\quad Sc = \frac{\mu_0}{D_m \rho_f},\quad Gr = \frac{\rho_f\, g\, \gamma_f\, \tilde{R}_0^2 (\tilde{T}_w-\tilde{T}_0)}{\tilde{u}_e \mu_0},\quad Nr = \frac{16\sigma_e \tilde{T}_0^3}{3k_f k_e},\quad Gr = \frac{\rho_f\, g\, \gamma_f\, \tilde{R}_0^2 (\tilde{C}_w-\tilde{C}_0)}{\tilde{u}_e \mu_0},\ Pr = \frac{(C_p)_f \mu_0}{k_f},\quad Re = \frac{\rho_f\, \tilde{u}_e\, \tilde{R}_0}{\mu_0},\quad Da = \frac{k_p}{\tilde{R}_0^2},\quad M^2 = \frac{\sigma_f\, \tilde{R}_0^2 \tilde{B}_0^2}{\mu_0},\ Ke = \frac{\tilde{R}_0}{\lambda_D}, \tilde{\delta} = \frac{\delta}{\tilde{R}_0}, \epsilon = \frac{\tilde{R}_0}{\tilde{z}_l}, \psi = \frac{\tilde{\psi}}{\psi_w} \tag{10}$$

The set of Equations (1) to (9) is written in dimensionless form using the dimensionless variables. The converted equations are given as

$$\tilde{R}(\tilde{z}) = \begin{cases} 1 - 2\delta \frac{h^{(h/(h-1))}}{h-1} H_4\,; & d \le z \le d+1 \\ 1 - \frac{3\delta}{8}\, H_5 \quad ; & d+2 \le z \le d+3 \\ 1 - \delta H_6 \quad ; & d+3 \le z \le d+4 \\ 1 \quad ; & otherwise \end{cases} \tag{11}$$

where, $\xi_e = z - d - 2$ and $h = 50$,

$H_4 = (11(z-d) - (z-d)^h)$, $H_5 = [11(\xi_e) - 47(\xi_e)^2 + 72(\xi_e)^3 - 36(\xi_e)^4]$, $H_6 = sin[\pi(z-d-3)]$

$$\delta\left(\frac{\partial u}{\partial r} + \frac{u}{u}\right) + \varepsilon \frac{\partial w}{\partial z} = 0 \tag{12}$$

$$+\varepsilon^2 \left(\frac{\partial}{\partial z}(S_{rz}) + \frac{1}{r}\frac{\partial}{\partial r}(S_{rr})\right) - \delta\, \varepsilon^2 \frac{\mu_{hnf}}{\mu_0}\frac{u}{r^2} \tag{13}$$

$$\frac{\rho_{hnf}}{\rho_f} Re\left(\frac{\partial w}{\partial t} + \delta\varepsilon u \frac{\partial w}{\partial r} + \varepsilon w \frac{\partial w}{\partial z}\right) = -\frac{\partial p}{\partial z} + \varepsilon^2 \left(\frac{\partial}{\partial z}(S_{zz})\right) + \frac{1}{r}\frac{\partial}{\partial r}(S_{rz}) - \frac{\mu_{hnf}}{\mu_0}\frac{w}{Da} + Ke^2 \psi(r) - \frac{\sigma_{hnf}}{\sigma_f} M^2 w + \frac{(\gamma\rho)_{hnf}}{(\gamma\rho)_f} Gr\ \theta + \frac{(\gamma\rho)_{hnf}}{(\gamma\rho)_f} Gm\ \phi + G(t) \tag{14}$$

$$\frac{(\rho C_p)_{hnf}}{(\rho C_p)_f} Pr\ Re\left(\frac{\partial \theta}{\partial t} + \delta\varepsilon\, u \frac{\partial \theta}{\partial r} + \varepsilon\, w \frac{\partial \theta}{\partial z}\right) = \frac{1}{k_f}\frac{1}{r}\frac{\partial}{\partial r}\left(k_{hnf}(1+\alpha_1\theta) r \frac{\partial \theta}{\partial r}\right) + \frac{\varepsilon^2}{k_f}\frac{\partial}{\partial z}\left(k_{hnf}(1+\alpha_1\theta)\frac{\partial \theta}{\partial z}\right) + Nr \frac{\partial^2 \theta}{\partial r^2} + \frac{\sigma_{hnf}}{\sigma_f} M^2\, Ec\, w^2 + \frac{\mu_{hnf}}{\mu_0}\left[\left(\delta\varepsilon \frac{\partial u}{\partial r}\right)^2 + \left(\delta\varepsilon \frac{u}{r}\right)^2 + \left(\varepsilon \frac{\partial w}{\partial z}\right)^2 + \frac{1}{2}\left(\delta\varepsilon^2 \frac{\partial u}{\partial z} + \frac{\partial w}{\partial r}\right)^2\right] \tag{15}$$

$$Sc\ Re\left(\frac{\partial \phi}{\partial t} + \delta\varepsilon u \frac{\partial \phi}{\partial r} + \varepsilon w \frac{\partial \phi}{\partial z}\right) = \left(\frac{\partial^2 \phi}{\partial r^2} + \frac{1}{r}\frac{\partial \phi}{\partial r} + \varepsilon^2 \frac{\partial^2 \phi}{\partial z^2}\right) - k_1 Sc(1+\alpha\theta)^q exp\left[-\frac{E_b}{(1+\alpha\theta)}\right]\phi \tag{16}$$

$$S_{rr} = \frac{\mu_{hnf}}{\mu_0}\delta\left[1 - m\zeta\left\{\left(\varepsilon^2\delta\frac{\partial u}{\partial z} + \frac{\partial w}{\partial r}\right)^2 + 2\left(\left(\delta\varepsilon\frac{\partial u}{\partial r}\right)^2 + \left(\delta\varepsilon\frac{u}{r}\right)^2 + \left(\varepsilon\frac{\partial w}{\partial z}\right)^2\right)\right\}\right]\left[2\frac{\partial u}{\partial r}\right] \tag{17}$$

$$S_{rz} = \frac{\mu_{hnf}}{\mu_0}\left[1 - m\zeta\left\{\left(\varepsilon^2\delta\frac{\partial u}{\partial z} + \frac{\partial w}{\partial r}\right)^2 + 2\left(\left(\delta\varepsilon\frac{\partial u}{\partial r}\right)^2 + \left(\delta\varepsilon\frac{u}{r}\right)^2 + \left(\varepsilon\frac{\partial w}{\partial z}\right)^2\right)\right\}\right]\left[\frac{\partial w}{\partial r} + \delta\varepsilon^2\frac{\partial u}{\partial z}\right] \tag{18}$$

$$S_{zz} = \frac{\mu_{hnf}}{\mu_0}\left[1 - m\zeta\left\{\left(\varepsilon^2\delta\frac{\partial u}{\partial z} + \frac{\partial w}{\partial r}\right)^2 + 2\left(\left(\delta\varepsilon\frac{\partial u}{\partial r}\right)^2 + \left(\delta\varepsilon\frac{u}{r}\right)^2 + \left(\varepsilon\frac{\partial w}{\partial z}\right)^2\right)\right\}\right]\left[2\frac{\partial w}{\partial z}\right] \tag{19}$$

Here, employ two physical simplifications to describe a mildly stenosed artery. First, authors assume that the stenosis height is much smaller than the normal artery radius, meaning the narrowing is quite shallow compared to the artery size. Second, the same order as the length over which the stenosis extends, in other words, the width and length of the narrowed region are comparable. According to these assumptions, the governing equations describing blood flow are transformed into a simpler set, as shown below.

$$\frac{\partial w}{\partial z} = 0 \tag{20}$$

$$\frac{\partial p}{\partial r} = 0 \tag{21}$$

$$\frac{\rho_{hnf}}{\rho_f} Re \frac{\partial w}{\partial t} = -\frac{\partial p}{\partial z} + \frac{1}{r}\frac{\partial}{\partial r}(S_{rz}) - \frac{\mu_{hnf}}{\mu_0}\frac{w}{Da} + Ke^2\psi(r) - \frac{\sigma_{hnf}}{\sigma_f} M^2 w + \frac{(\gamma\rho)_{hnf}}{(\gamma\rho)_f} Gr\ \theta + \frac{(\gamma\rho)_{hnf}}{(\gamma\rho)_f} Gm\ \phi + G(t) \tag{22}$$

$$\frac{(\rho C_p)_{hnf}}{(\rho C_p)_f} Pr\ Re \frac{\partial \theta}{\partial t} = \frac{1}{k_f}\frac{1}{r}\frac{\partial}{\partial r}\left(k_{hnf}(1+\alpha_1\theta) r \frac{\partial \theta}{\partial r}\right) + Nr \frac{\partial^2 \theta}{\partial r^2} + \frac{\sigma_{hnf}}{\sigma_f} M^2\ Ec\ w^2 + \frac{\mu_{hnf}}{\mu_0}\frac{1}{2}\left(\frac{\partial w}{\partial r}\right)^2 \tag{23}$$

$$Sc\ Re \frac{\partial \phi}{\partial t} = \frac{\partial^2 \phi}{\partial r^2} + \frac{1}{r}\frac{\partial \phi}{\partial r} - k_1 Sc(1+\alpha\theta)^q exp\left[-\frac{E_n}{(1+\alpha\theta)}\right]\phi \tag{24}$$

$$S_{rr} = 0 \tag{25}$$

$$S_{rz} = \frac{\mu_{hnf}}{\mu_0}\left[1 - m\zeta\left(\frac{\partial w}{\partial r}\right)^2\right]\frac{\partial w}{\partial r} \tag{26}$$

$$S_{zz} = 0 \tag{27}$$

2.6. Radial Coordinate Transformation

The radial coordinate transformation $x = \frac{r}{R(z)}$ In a stenosed artery, this transformation in flow equations is important because it normalizes the radial position within the stenosed artery relative to its radius $R(z)$, which varies due to the narrowing (stenosis). This transformation simplifies the governing partial differential equations by mapping the changing arterial geometry onto a fixed normalized coordinate system from 0 to 1. After that, equations (22), (23), and (24) become as follows:

$$\frac{\rho_{hnf}}{\rho_f} Re \frac{\partial w}{\partial t} = -\frac{\partial p}{\partial z} + \frac{1}{R^3}\frac{1}{x}\frac{\partial}{\partial x}\left[\frac{\mu_{hnf}}{\mu_0}\left(1 - m\zeta\frac{1}{R^2}\left(\frac{\partial w}{\partial x}\right)^2\right)\frac{\partial w}{\partial x}\right] - \frac{\mu_{hnf}}{\mu_0}\frac{w}{Da} + Ke^2\psi(xR) - \frac{\sigma_{hnf}}{\sigma_f} M^2 w + \frac{(\gamma\rho)_{hnf}}{(\gamma\rho)_f} Gr\ \theta + \frac{(\gamma\rho)_{hnf}}{(\gamma\rho)_f} Gm\ \phi + G(t) \tag{28}$$

$$\frac{(\rho C_p)_{hnf}}{(\rho C_p)_f} Pr\ Re \frac{\partial \theta}{\partial t} = \frac{1}{k_f}\frac{1}{R^2}\frac{1}{x}\frac{\partial}{\partial x}\left(k_{hnf}(1+\alpha_1\theta) x \frac{\partial \theta}{\partial x}\right) + Nr \frac{1}{R^2}\frac{\partial^2 \theta}{\partial x^2} + \frac{\sigma_{hnf}}{\sigma_f} M^2\ Ec\ w^2 + \frac{\mu_{hnf}}{\mu_0}\frac{1}{2}\frac{1}{R^2}\left(\frac{\partial w}{\partial x}\right)^2 \tag{29}$$

$$Sc\ Re \frac{\partial \phi}{\partial t} = \frac{1}{R^2}\frac{\partial^2 \phi}{\partial x^2} + \frac{1}{R^2}\frac{1}{x}\frac{\partial \phi}{\partial x} - k_1 Sc(1+\alpha\theta)^q exp\left[-\frac{E_n}{(1+\alpha\theta)}\right]\phi \tag{30}$$

3. Methods of Solution

3.1. Stability Analysis and Model Convergence

These governing equations are highly nonlinear. Therefore, the analytical solution is very complicated. So, because of the simplicity and straightforward implementation, the authors implemented the FTCS scheme for solving the equations. The explicit FTCS schemes are central in space and forward in time; the detailed explanation of this scheme is given by Hoffman and Chiang [20] and Smith [13].

In the research field, several researchers (Yadav and Singh [30]; Tripathi et al. [18]) used this scheme in their research. Consequently, for the convergent and stable solution, the time step is 0.0001 and the spatial step size is 0.025. The condition of stability is explained by Yadav and Singh [30], which is $\frac{\Delta t}{Re\ \Delta x^2} \leq \frac{1}{2}$.

In this scheme,

$\frac{\partial w}{\partial x} \cong \frac{w_{i+1,j} - w_{i-1,j}}{2\ \Delta x}$, $\frac{\partial w}{\partial t} \cong \frac{w_{i,j+1} - w_{i,j}}{\Delta t}$, $\frac{\partial^2 w}{\partial x^2} \cong \frac{w_{i+1,j} - 2\ w_{i,j} + w_{i-1,j}}{\Delta x^2}$

Initial and Boundary conditions in the discretized form as,

$w_{i,1} = 0, \theta_{i,1} = 0, \phi_{i,1} = 0$ at $t = 0$
$w_{i+1,j} = w_{i,j}, \theta_{i+1,j} = \theta_{i,j}, \phi_{i+1,j} = \phi_{i,j}$ at $x = 0$
$w_{N+1,j} = 0,\ \theta_{N+1,j} = 1,\ \phi_{N+1,j} = 0$ at $x = 1 w_{i,j+1} = w_{i,j} +$

$$\frac{\rho_f}{\rho_{hnf}}\frac{1}{Re}\Delta t\left\{B_1\left(1 + e\ cos(c_1(j-1)\Delta t)\right) + \frac{1}{R^3}\frac{(1-\beta_0\theta_{i,j})}{x_i}\left[\frac{w_{i+1,j} - 2\ w_{i,j} + w_{i-1,j}}{\Delta x^2} - \frac{3m\zeta}{R^2}\left(\left(\frac{w_{i+1,j} - w_{i-1,j}}{2\ \Delta x}\right)^2\left(\frac{w_{i+1,j} - 2\ w_{i,j} + w_{i-1,j}}{\Delta x^2}\right)\right)\right] - \frac{\beta_0}{x_i}\left[\left(\frac{w_{i+1,j} - w_{i-1,j}}{2\ \Delta x}\right) - \frac{m\zeta}{R^2}\left(\frac{w_{i+1,j} - w_{i-1,j}}{2\ \Delta x}\right)^3\right]\left(\frac{\theta_{i+1,j} - \theta_{i-1,j}}{2\ \Delta x}\right) - \frac{\mu_{hnf}}{\mu_0}\frac{w_{i,j}}{Da} + Ke^2\psi(x_i R) - \frac{\sigma_{hnf}}{\sigma_f} M^2 w_{i,j} + \frac{(\gamma\rho)_{hnf}}{(\gamma\rho)_f} Gr\ \theta_{i,j} + \frac{(\gamma\rho)_{hnf}}{(\gamma\rho)_f} Gm\ \phi_{i,j} + \frac{\rho_{hnf}}{\rho_f} B_1 cos(c_2(j-1)\Delta t + \alpha)\right\} \tag{31}$$

$$\theta_{i,j+1} = \theta_{i,j} + \frac{(\rho C_p)_f}{(\rho C_p)_{hnf}}\frac{1}{PrRe}\Delta t\left\{\frac{k_{hnf}}{k_f}\frac{1}{R^2}\left[\frac{(1+\alpha_1\theta_{i,j})}{x_i}\left(\frac{\theta_{i+1,j} - \theta_{i-1,j}}{2\ \Delta x}\right) + \alpha_1\left(\frac{\theta_{i+1,j} - \theta_{i-1,j}}{2\ \Delta x}\right) + \left(1 + \alpha_1\theta_{i,j}\right)\left(\frac{\theta_{i+1,j} - 2\ \theta_{i,j} + \theta_{i-1,j}}{\Delta x^2}\right)\right] + Nr\frac{1}{R^2}\left(\frac{\theta_{i+1,j} - 2\ \theta_{i,j} + \theta_{i-1,j}}{\Delta x^2}\right) + \frac{\sigma_{hnf}}{\sigma_f} M^2\ Ec\ {w_{i,j}}^2 + \frac{\mu_{hnf}}{\mu_0}\frac{1}{2}\frac{1}{R^2}\left(\frac{w_{i+1,j} - w_{i-1,j}}{2\ \Delta x}\right)^2\right\} \tag{32}$$

$$\phi_{i,j+1} = \phi_{i,j} + \frac{1}{Sc\ Re}\Delta t\left\{\frac{1}{R^2}\left[\left(\frac{\phi_{i+1,j} - 2\ \phi_{i,j} + \phi_{i-1,j}}{\Delta x^2}\right) + \frac{1}{x_i}\left(\frac{\phi_{i+1,j} - \phi_{i-1,j}}{2\ \Delta x}\right)\right] - k_1 Sc\left(1 + \alpha\theta_{i,j}\right)^q exp\left[-\frac{E_n}{(1+\alpha\theta_{i,j})}\right]\phi_{i,j}\right\} \tag{33}$$

3.2. Validation

In the phase of validation, the result of validation is shown in Figure 2. This model is validated with the research of Yadav and Singh [30].

The validation happens when the Arrhenius activation energy is converted into a constant chemical reaction parameter, as mentioned in the work of Yadav and Singh [30].

The temperature-dependent thermal conductivity is taken to be independent of the temperature, and the Reynolds viscosity model is replaced by the Einstein viscosity model.

3.3. Mesh Independence Analysis

The mesh independence test is an important methodology in numerical simulation, including finite difference methods and finite element methods, to ensure that the results are not dependent on the mesh size or mesh density. In the paper, check the mesh independence using different sizes of the mesh. Table 3 has been prepared under this section to show the calculations of concentration at different mesh refinements. The values in the Table 3 show that there is an insignificant difference in error between the 41×10001 and 44×11001 mesh sizes in determining the magnitude of the concentration. In turn, the mesh size of 40×10001 has been chosen to obtain the numerical results.

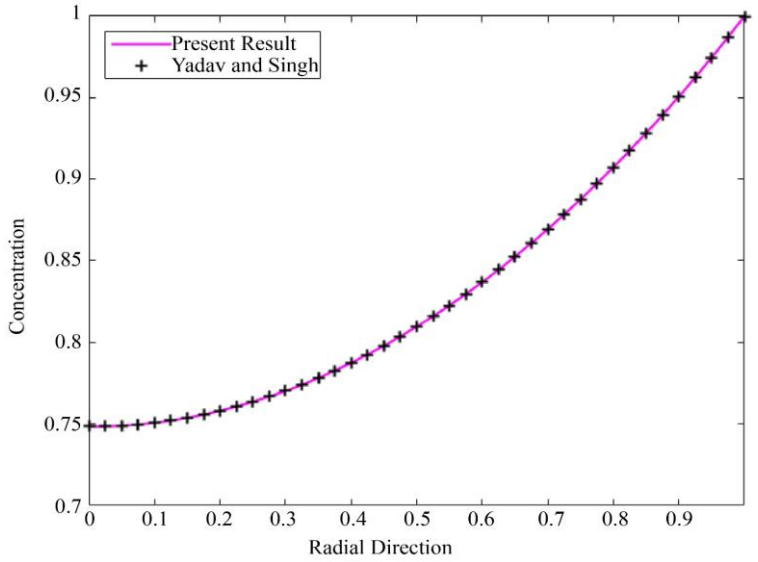

Fig. 2 Comparison of concentration profile with the present result and Yadav and Singh [23] for overlapping stenosis and $Re = 2$

4. Results and Discussion

The current hybrid nanofluid model investigates the blood flow behavior with variation of the different flow parameters. The present research introduces a novel mathematical model that investigates blood flow dynamics in an artery featuring three different types of stenosis, namely irregular, overlapping, and elliptical at the distinct locations, addressing a combination of variable thermal conductivity, Reynolds viscosity model, uniform magnetic field, electrical field, and Arrhenius activation energy effects over time $t = 1$. The suspension of Ag and TiO_2 nanoparticles are incorporated to intensify heat and mass transfer and optimize drug delivery mechanisms with multiple stenoses in a single straight artery.

The default values of the parameters for this model are as follows: Reynolds number (2), Schmidt number (0.5), activation energy parameter (2), thermal Grashof number (0.3), Solutal Grashof number (0.3), Prandtl number (14), radiation parameter (1), Eckert number (0.5), electrokinetic parameter (0.6), Darcy number (0.3), Schmidt number (0.5), Hartmann number (2), $k_1 = 0.8$, $q = 2$, $\delta = 0.2$, $B_1 = 1.14$, $B_2 = 1$, $e = 0.2$, $c_1 = 1$, $c_2 = 1$, $\zeta = 0.1$,$\alpha = \pi/4$, $\beta_0 = 0.2$, $m = 2$, $d = 1$ (Sharma and Gandhi [8], Tripathi and Sharma [9], Glili et al. [15], Tripathi et al. [17], Tripathi et al. [19], Coronel et al. [23], Ahammad and Talea [28], Yadav and Singh [30], Manchi and Ponalagusamy [35]).

Figure 3 represents the velocity profile at the three different locations of the artery ($z = 1.5$, $z = 3.5$, and $z = 4.5$). The Darcy number is related to fluid dynamics and porous media theory. Therefore, the Da is directly proportional to permeability. As the Da increases, this means increasing the permeability of the porous medium (plaque). The plaque became leakier. The pores within it are larger and more interconnected. There is less resistance to the flow of Blood passing through it. So, the velocity increases as the Darcy number increases from 0.3 to 1. The second finding is that the velocity profile is higher in the elliptical shape of the stenosis in the artery at $z = 4.5$ as compared to $z = 1.5$ (irregular shape of the stenosis) and $z = 3.5$ (overlapping shape of the stenosis).

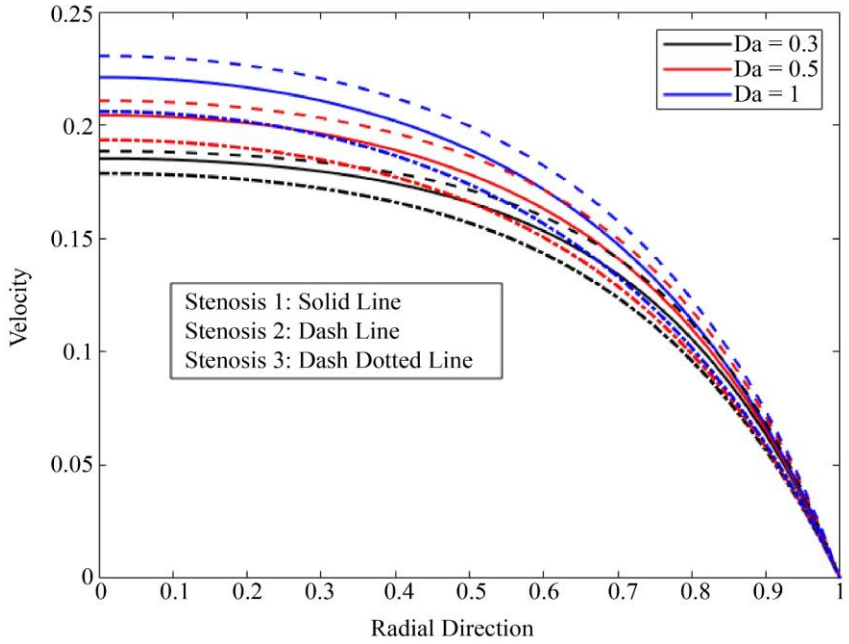

Fig. 3 Effect of Darcy number (0.3, 0.5, and 1) variation on velocity profile for the three different stenoses (irregular (stenosis 1), overlapping (stenosis 2), and elliptical (stenosis 3)) at distinct locations ($z = 1.5$, $z = 3.5$, and $z = 4.5$) over time $t = 1$.

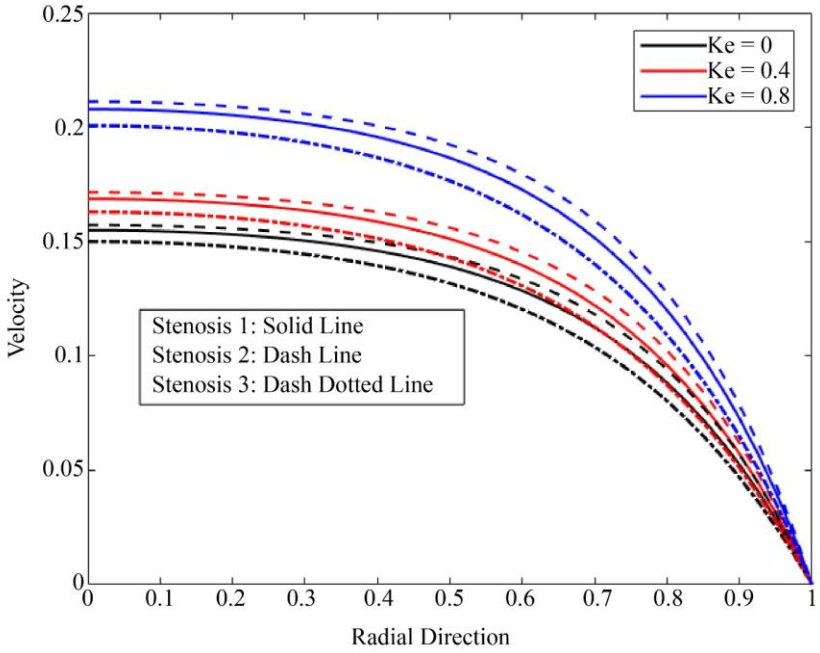

Fig. 4 Effect of kinetic parameter (0, 0.4, and 0.8) variation on velocity profile for the three different stenoses (irregular (stenosis 1), overlapping (stenosis 2), and elliptical (stenosis 3)) at distinct locations ($z = 1.5$, $z = 3.5$, and $z = 4.5$) over time $t = 1$.

Figure 4 depicts the impact of the Ke at the three different locations of the artery. The electrokinetic parameter is related to the artery radius and Debye length. As the value of Ke increases from 0 to 0.8, the velocity increases. This happens due to a natural phenomenon, which is that a reduction in the electrical double layer thickness enhances the electroosmotic driving forces while simultaneously reducing the resistance to fluid (Blood) motion within the medium. The electrical double layer forces at the solid-liquid (surface and blood) interface due to the accumulation of counter ions near the charged surface, and its thickness is characterised by the Debye length.

Figure 5 illustrates the velocity profile at the three different locations of the artery as a function of the Nr. It is concluded from the figure that the impact of $Nr = 5$ is the same near the centre of the artery for the irregular and

overlapping segment of the artery. As a consequence, the velocity increased as the increment in the radiation parameter from 1 to 3. It happens due to thermal energy because radiation acts as an additional heat source, and the absorbed energy directly increases the thermal (internal) energy of the Blood. As the thermal energy rises, the random motion of the blood molecules intensifies, which enhances the rate of heat transfer within the fluid (Blood).

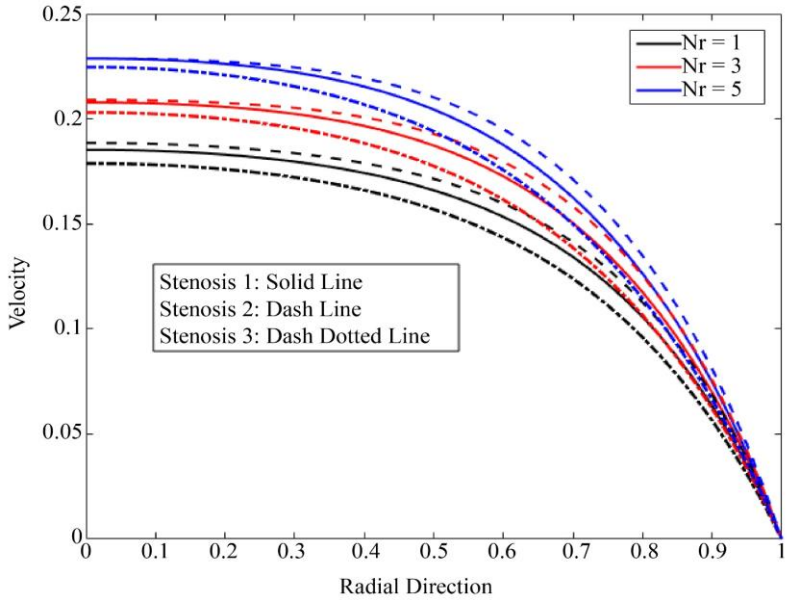

Fig. 5 Effect of radiation parameter (1, 3, and 5) variation on velocity profile for the three different stenoses (irregular (stenosis 1), overlapping (stenosis 2), and elliptical (stenosis 3)) at distinct locations ($z = 1.5$, $z = 3.5$, and $z = 4.5$) for the time $t = 1$.

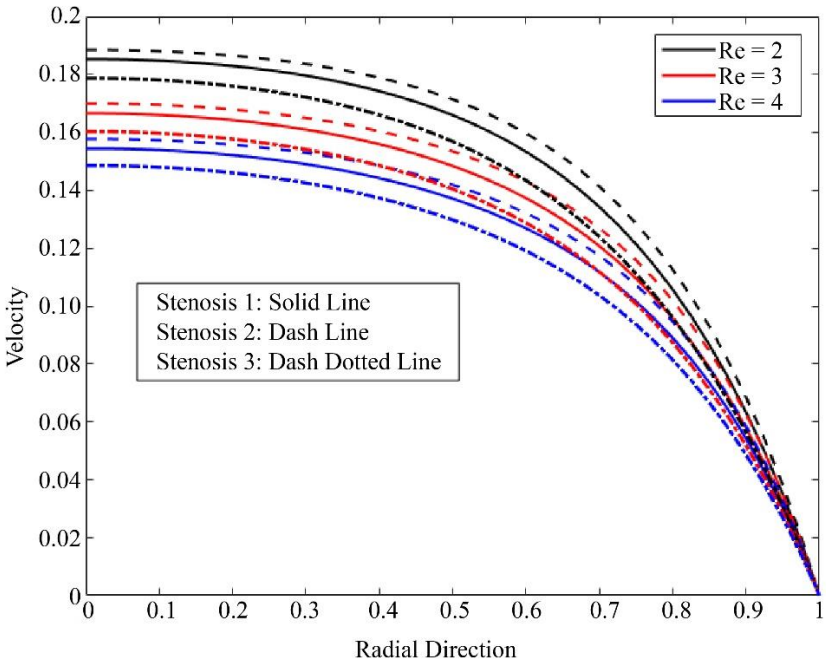

Fig. 6 Effect of Reynolds number (2, 3, and 4) variation on velocity profile for the three different stenoses (irregular (stenosis 1), overlapping (stenosis 2), and elliptical (stenosis 3)) at distinct locations ($z = 1.5$, $z = 3.5$, and $z = 4.5$) for the time $t = 1$.

Figure 6 represents the velocity profile for several values of Reynolds at the three different types of stenosis in the single straight artery. It is concluded from the figure that the velocity of Blood declines as the Reynolds number increases. Also, notice that the high velocity in the overlapping segment of the artery is compared to the irregular and elliptical. It means the viscous force is weak in the overlapping segment as compared to the irregular and elliptical segment. The impact of the magnetic number M on the velocity profile is represented in Figure 7. It is concluded from the Figure that the velocity

declines as the magnetic number increases. It is also noticed that near the centre of the artery, there is very little difference in the artery for all the stenotic segments, and a greater difference is noticed for the value of $M = 1$. Figure 8 shows the velocity profile with the impact of the concentration of the hybrid nanoparticles.

It is noticed from the figure that increasing the nanoparticle volume fraction for the hybrid nanofluid results in a decline in the velocity. Figure 8 illustrates the velocity influenced by the concentration of hybrid nanoparticles. The figure indicates that when the volume fraction of nanoparticles in the hybrid nanofluid increases, the velocity decreases.

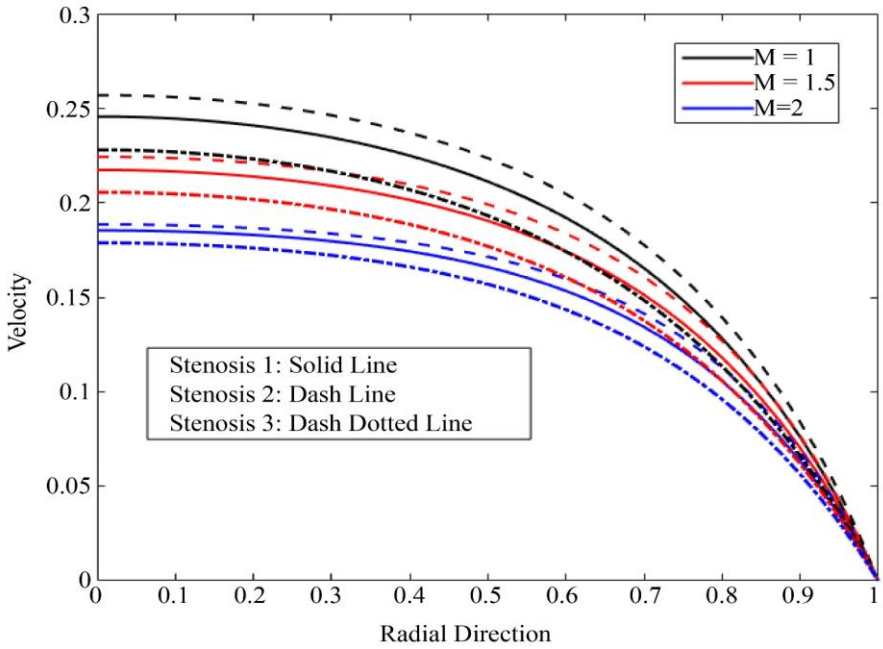

Fig. 7 Effect of magnetic number (1, 1. 5, and 2) variation on velocity profile for the three different stenoses (irregular (stenosis 1), overlapping (stenosis 2), and elliptical (stenosis 3)) at distinct locations ($z = 1.5$, $z = 3.5$, and $z = 4.5$) for the time $t = 1$

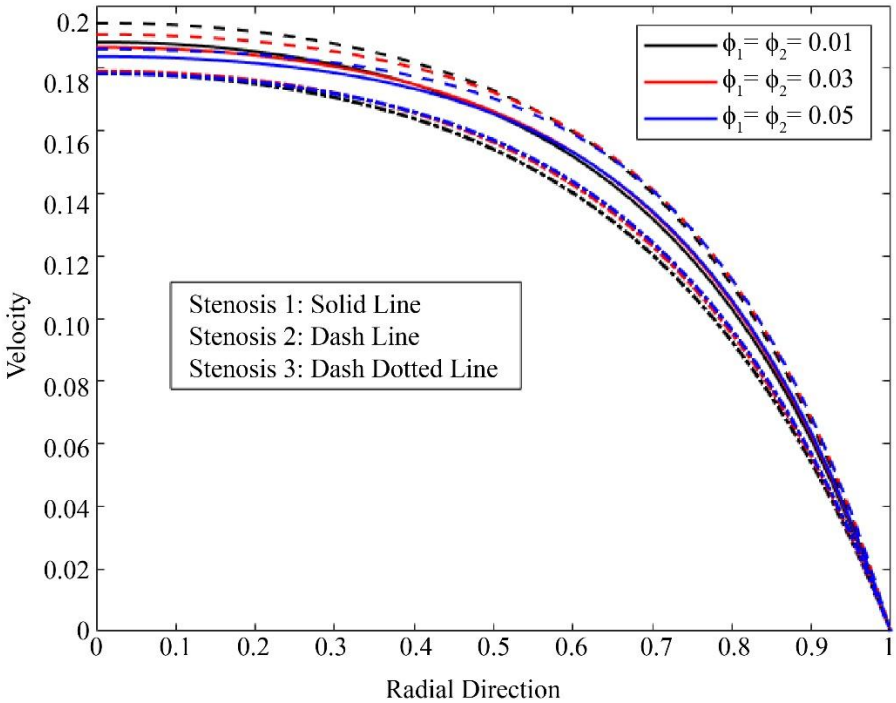

Fig. 8 Effect of volume fraction concentration of hybrid nanoparticles (0. 01, 0. 03, and 0. 05) variation on velocity profile for the three different stenoses (irregular (stenosis 1), overlapping (stenosis 2), and elliptical (stenosis 3)) at distinct locations ($z = 1.5$, $z = 3.5$, and $z = 4.5$) for the time $t = 1$.

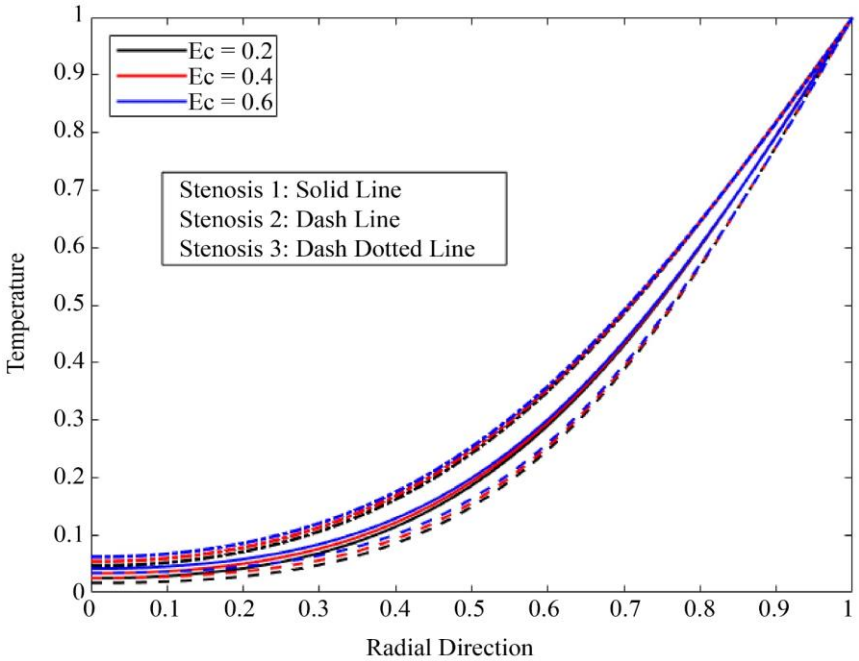

Fig. 9 Effect of Eckert number (0.2, 0.4, and 0.6) variation on temperature profile for the three different stenoses (irregular (stenosis 1), overlapping (stenosis 2), and elliptical (stenosis 3)) at distinct locations ($z = 1.5$, $z = 3.5$, and $z = 4.5$) for the time $t = 1$

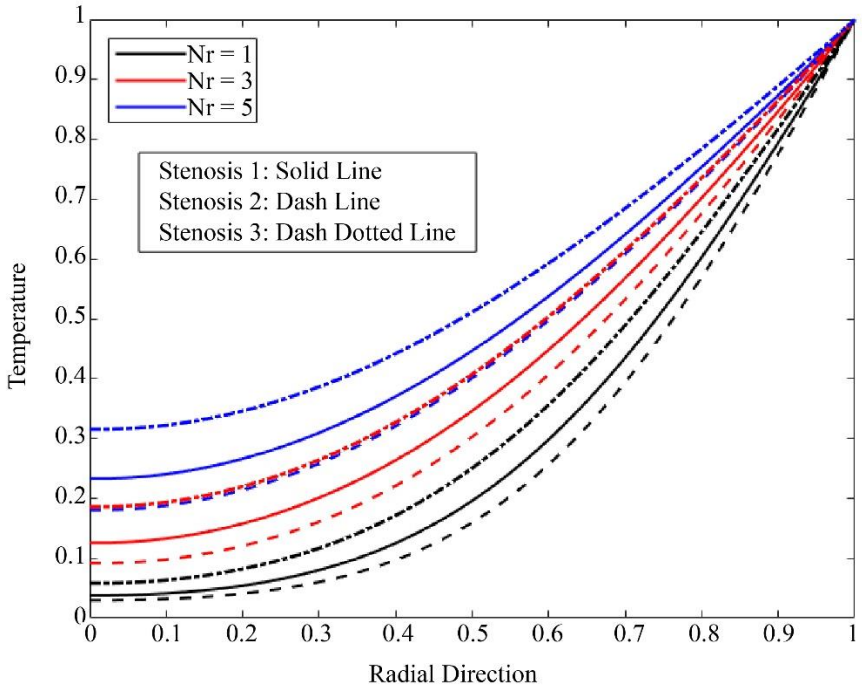

Fig. 10 Effect of radiation parameter (1, 3, and 5) variation on temperature profile for the three different stenoses (irregular (stenosis 1), overlapping (stenosis 2), and elliptical (stenosis 3)) at distinct locations ($z = 1.5$, $z = 3.5$, and $z = 4.5$) for the time $t = 1$

Figure 9 represents the impact on the temperature profile. The Figure concluded that temperature is accelerated as the value of Ec increases. The underlying physics of this phenomenon is that the Ec characterizes the ratio of the Blood's kinetic energy to thermal energy. A high Eckert number indicates that the kinetic energy of the fluid becomes more significant relative to the thermal energy. Consequently, when the Blood flows with steep velocity gradients, the viscous forces acting on the adjacent blood layers generate viscous dissipation. This dissipation of mechanical energy is irreversibly converted into internal energy in the form of heat, leading to a rise in blood temperature. It is also noted from the

figure that the blood temperature is higher in the elliptical shape stenosis compared to overlapping and irregular shapes of the stenosis near the arterial wall. Figure 10 illustrates the temperature profile at the three different locations of the artery as a function of the Nr. It is concluded from the figure that the temperature increased as the radiation parameter increment increased from 1 to 3. The effect of Pr variation on the temperature profile is displayed in Figure 11. From the figure, it is concluded that the variation of the Pr is from 7 to 21. The irregular stenosis in the axial direction occurs between 1 and 2, overlapping stenosis in the axial direction occurs between 3 and 4, and elliptical stenosis in the axial direction occurs between 4 and 5. The Pr indicates the ratio of the two physical parameters ('momentum diffusivity' and 'thermal diffusivity'). The temperature declines as the value of the Pr increases from 7 to 21. This happens due to generating a thicker momentum and a thinner boundary layer near the arterial wall of the stenosed artery. The effect of Re variation on temperature is demonstrated in Figure 12. From the figure, it is concluded that the variation of Reynolds is from 2 to 4. The Reynolds number significantly influences the temperature profile in blood flow through the artery, especially when Blood acts as a hybrid nanofluid containing silver and titanium oxide nanoparticles. An increment in the Reynolds number from 2 to 4 then enhances convective heat transfer by increasing fluid mixing and inertial forces, which decreases the temperature. The nanoparticles improve thermal conductivity and heat transfer within the Blood, further lowering the temperature profile by facilitating more efficient heat dissipation.

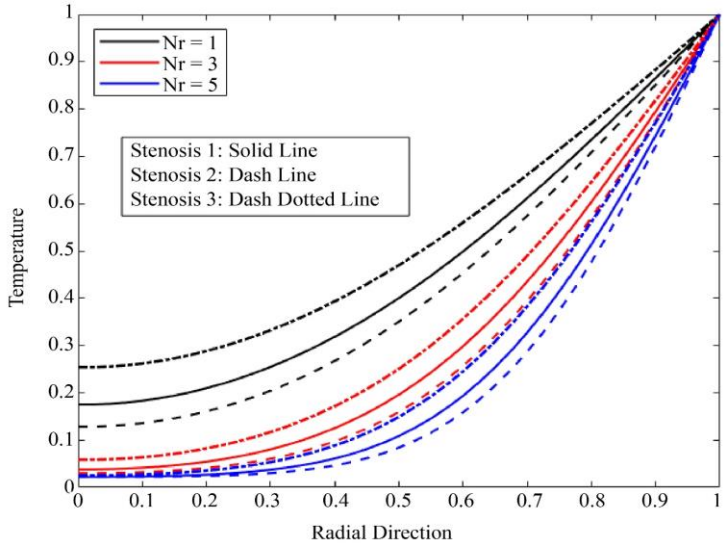

Fig. 11 Effect of Prandtl number (7, 14, and 21) variation on temperature profile for the three different stenoses (irregular (stenosis 1), overlapping (stenosis 2), and elliptical (stenosis 3)) at distinct locations ($z = 1.5$, $z = 3.5$, and $z = 4.5$) for the time $t = 1$.

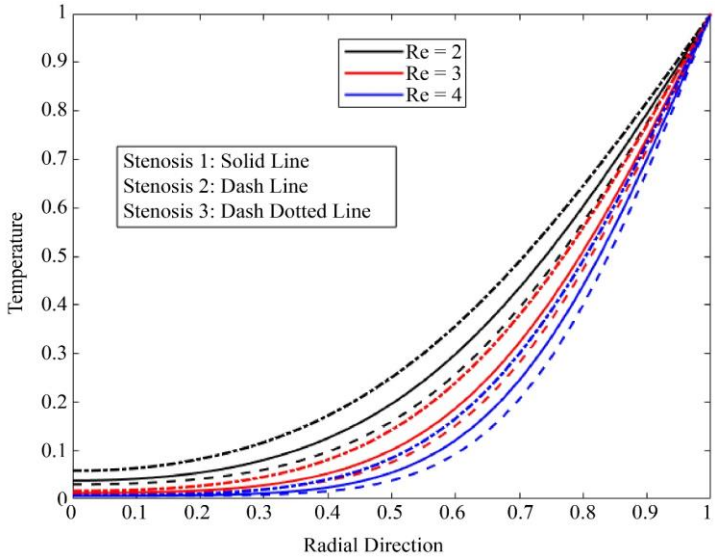

Fig. 12 Effect of Reynolds number (2, 3, and 4) variation on temperature profile for the three different stenoses (irregular (stenosis 1), overlapping (stenosis 2), and elliptical (stenosis 3)) at distinct locations ($z = 1.5$, $z = 3.5$, and $z = 4.5$) for the time $t = 1$

The effect of activation energy variation on the concentration profile is represented in Figure 13. From the Figure, it is noticed that the concentration profile enhances as the activation energy increases.

It indicates that the chemical reaction rate decreases due to the fact that a higher activation energy is required for the reactants to overcome the energy barrier to transform into products. The effect of Sc variation on the concentration profile is shown in Figure 14. If the Sc increases from 0.5 to 1.5, then the concentration decreases. The reason behind this is that the momentum diffusivity is faster than the mass diffusivity, leading to a thicker momentum boundary layer than the mass transfer boundary layer, which affects how species concentration varies within the fluid (Blood) domain or near the arterial wall.

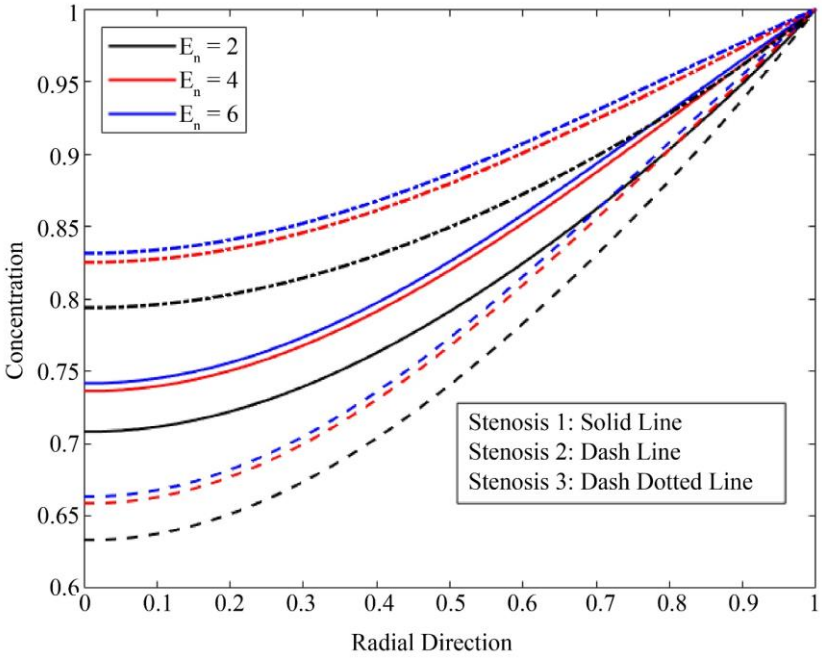

Fig. 13 Effect of activation energy (2, 4, and 6) variation on concentration profile for the three different stenoses (irregular (stenosis 1), overlapping (stenosis 2), and elliptical (stenosis 3)) at distinct locations ($z = 1.5$, $z = 3.5$, and $z = 4.5$) for the time $t = 1$

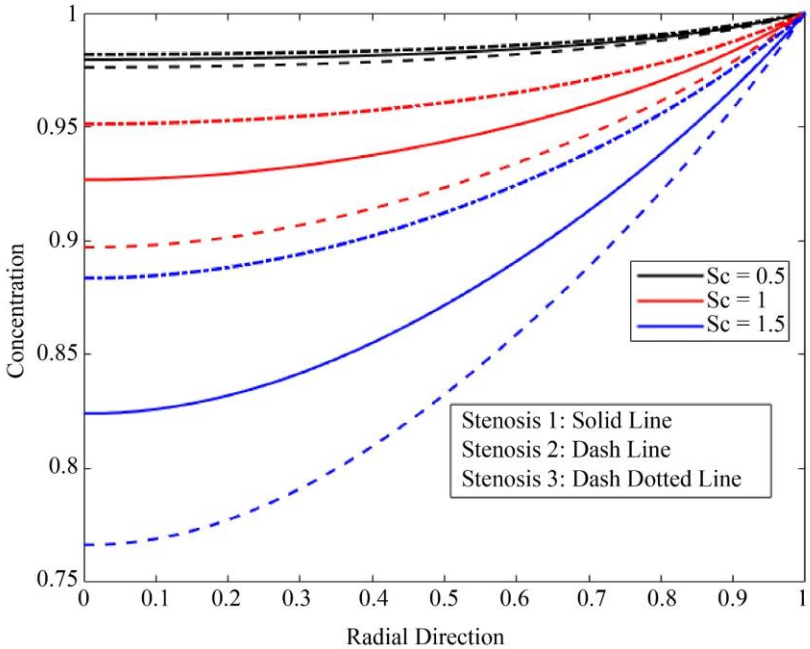

Fig. 14 Effect of Schmidt number (0.5, 1, and 1.5) variation on concentration profile for the three different stenoses (irregular (stenosis 1), overlapping (stenosis 2), and elliptical (stenosis 3)) at distinct locations ($z = 1.5$, $z = 3.5$, and $z = 4.5$) for the time $t = 1$.

Figure 15 demonstrated the effect of the depth of stenosis on wall shear stress for the three different stenosis over time $t = 1$. The depth of stenosis in the single straight artery at various locations significantly affects the wall shear stress, an essential parameter in vascular health and disease.

As the depth of the stenosis increases from 0.1 to 0.2, the cross-sectional area of the blood vessel narrows, causing accelerated blood flow in the artery and resulting in elevated wall shear stress in the stenotic segment. Figure 16 shows the effect of Sc variation on the Sh for the time $t = 1$. The Schmidt number indicates how momentum and mass diffusion occur in blood flow. It is noted from the figure that the Sh increases as the Sc increases from 0.5 to 1.1.

The natural phenomena that the mass transfer boundary layer is thin for the higher value of the Schmidt number, leading to increased Sherwood number and enhanced mass transport. Also, the lower value of the Schmidt number does not show much variation in the Sherwood number.

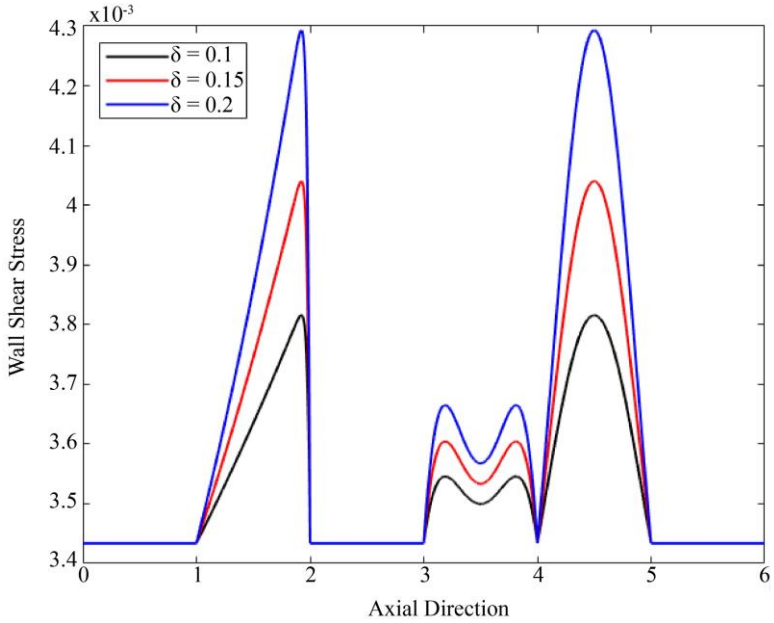

Fig. 15 Effect of depth of stenosis (0.1, 0.15, and 0.2) on wall shear stress for the three different stenoses (irregular (stenosis 1), overlapping (stenosis 2), and elliptical (stenosis 3)) for the time $t = 1$

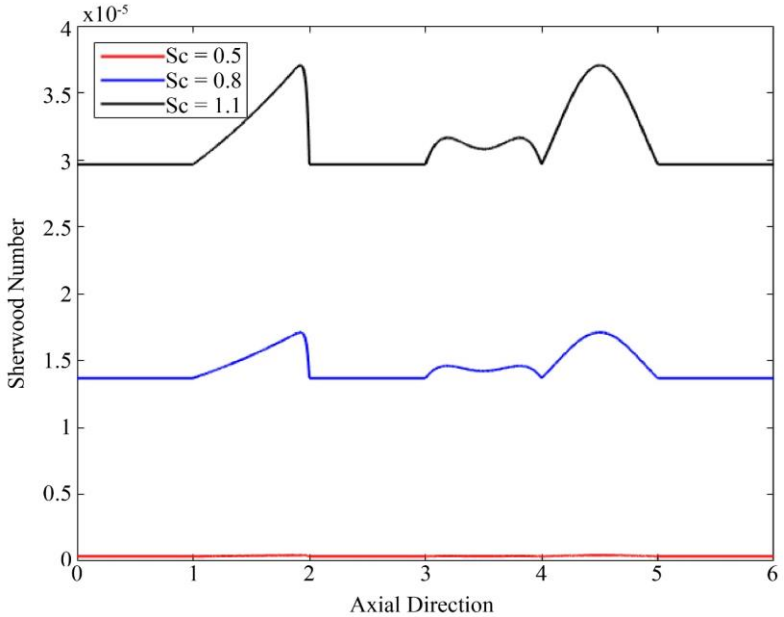

Fig. 16 Effect of Schmidt number (0.5, 0.8, and 1.1) variation on the Sherwood number for the three different stenoses (irregular (stenosis 1), overlapping (stenosis 2), and elliptical (stenosis 3)) for the time $t = 1$

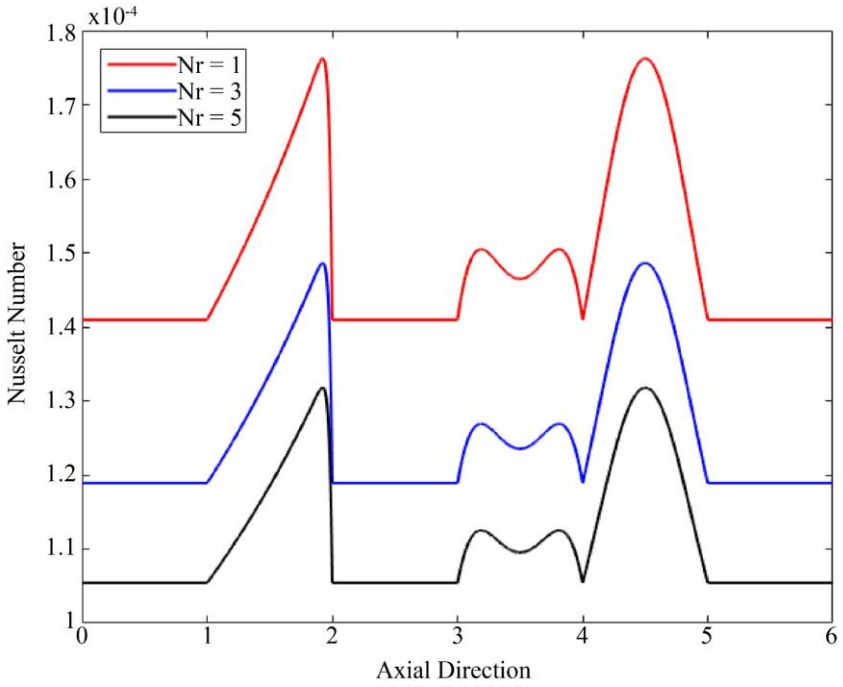

Fig. 17 Effect of radiation parameter (1, 2, and 3) variation on the Nusselt number for the three different stenoses (irregular (stenosis 1), overlapping (stenosis 2), and elliptical (stenosis 3)) for the time $t = 1$.

The effect of Nr variation on the Nu for the presence of the three different types of stenoses in the artery over time $t = 1$ is shown in Figure 17. It is concluded from the figure that the Nu declines as the enhanced radiation parameter increases from 1 to 3. This indicates reduced convective heat transfer while simultaneously increasing thermal boundary layer thickness. The effect of M variation on the resistance to flow over time $t = 1$ is represented in Figure 18. It is noted from the figure that the resistance to blood flow increases as the magnetic field parameter accelerates in MHD (magnetohydrodynamic) blood flow. A higher value of the magnetic field parameter represents a stronger transverse magnetic field acting on the electrically conducting Blood, producing a Lorentz force that opposes the motion of the fluid. This effect leads to increased resistance to flow due to the electromagnetic drag force.

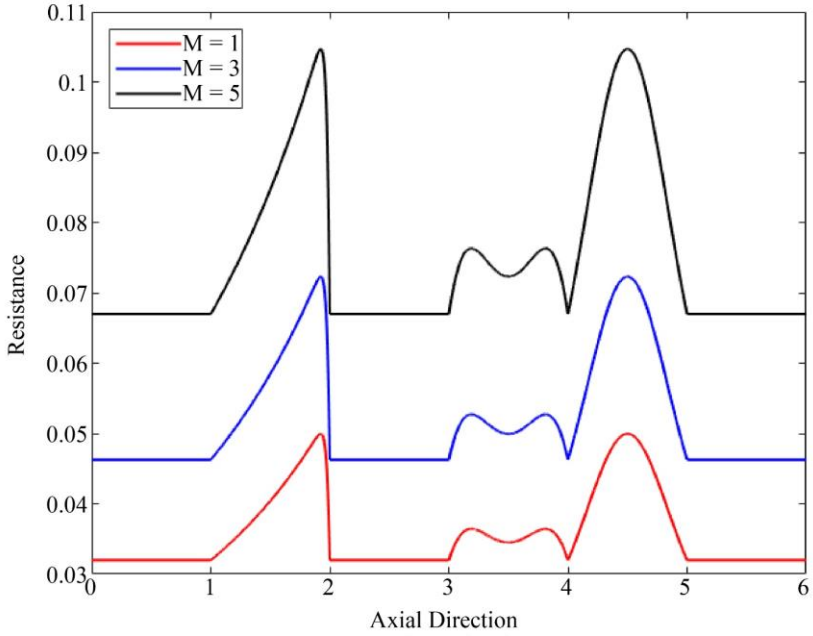

Fig. 18 Effect of magnetic field parameter (2, 3, and 4) variation in the resistance to flow for the three different stenoses (irregular (stenosis 1), overlapping (stenosis 2), and elliptical (stenosis 3)) over time $t = 1$

Figure 19 represents the contour plot for velocity, temperature, and concentration for pure Blood and hybrid nanofluid. Figure 19 (a) represents a velocity contour in pure Blood with a spectrum ranging from lower (blue) to higher (red) values. The velocity is higher near the centre of the artery and declines towards the arterial wall. Figure 19 (b) also represents the velocity contour with hybrid nanoparticles and its trend, similar to Figure 19 (a). Figure 19 (c) and Figure 19 (d) represent the temperature contour without and with nanoparticles, respectively, and the temperature is higher near the arterial wall and lower towards the centre of the artery. Similar patterns for the concentration contour in Figure 19 (e) and Figure 19 (f).

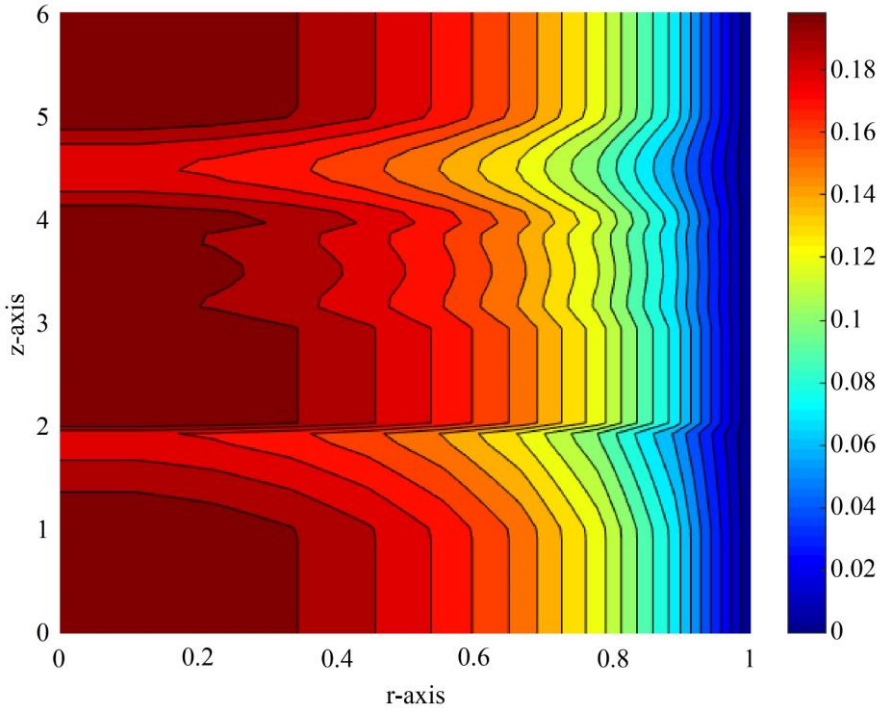

(a)

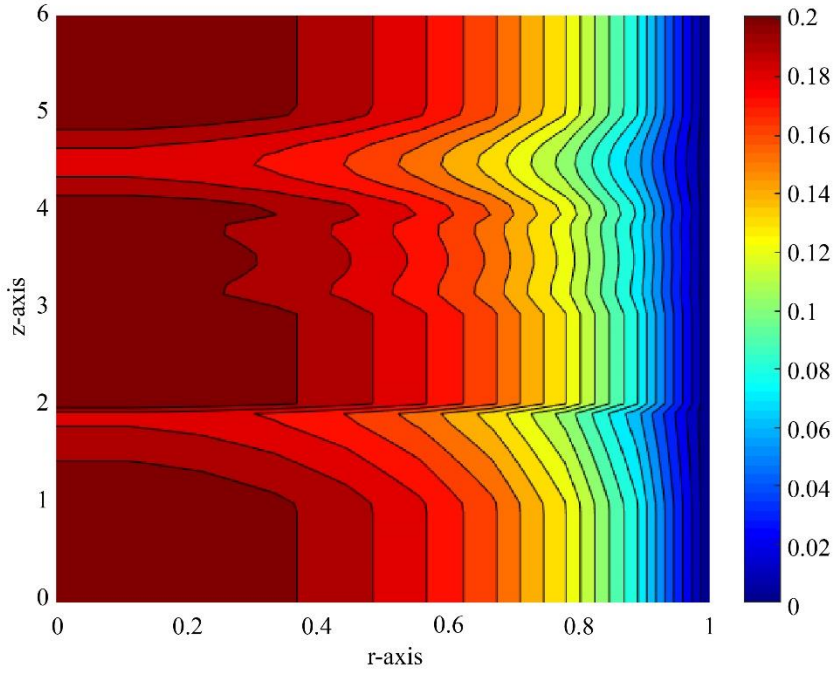

(b)

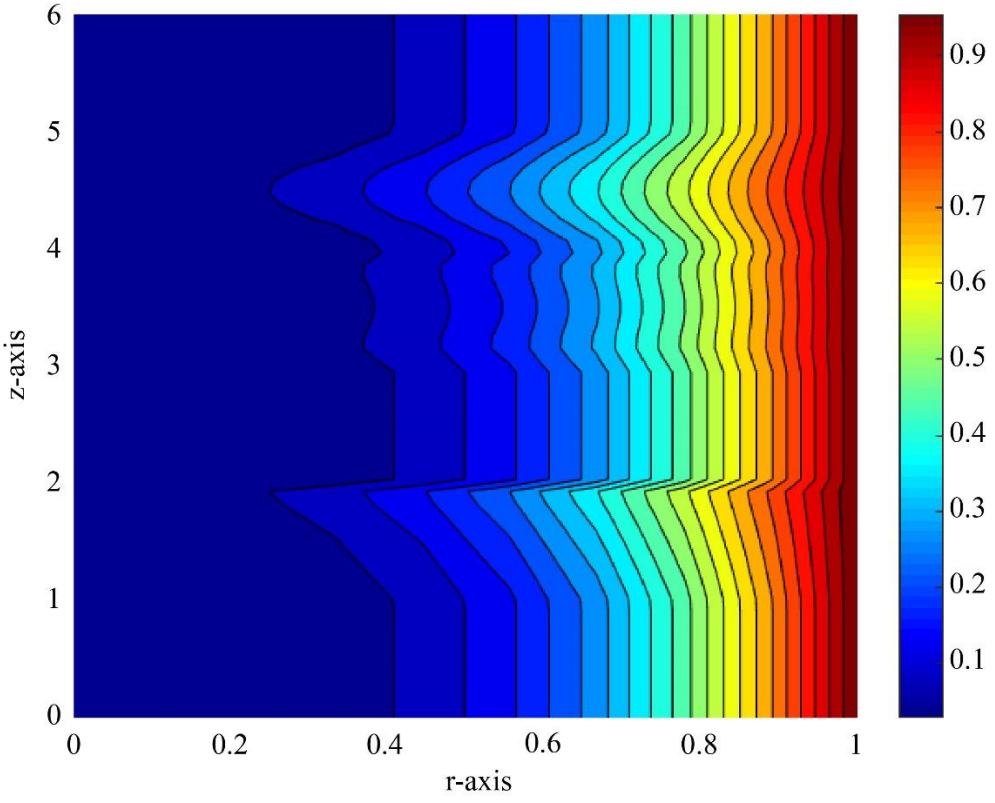
z-axis
r-axis
0
1
2
3
4
5
6
0.2
0.4
0.6
0.8
0.9
0.7
0.5
0.3
0.1

(c)

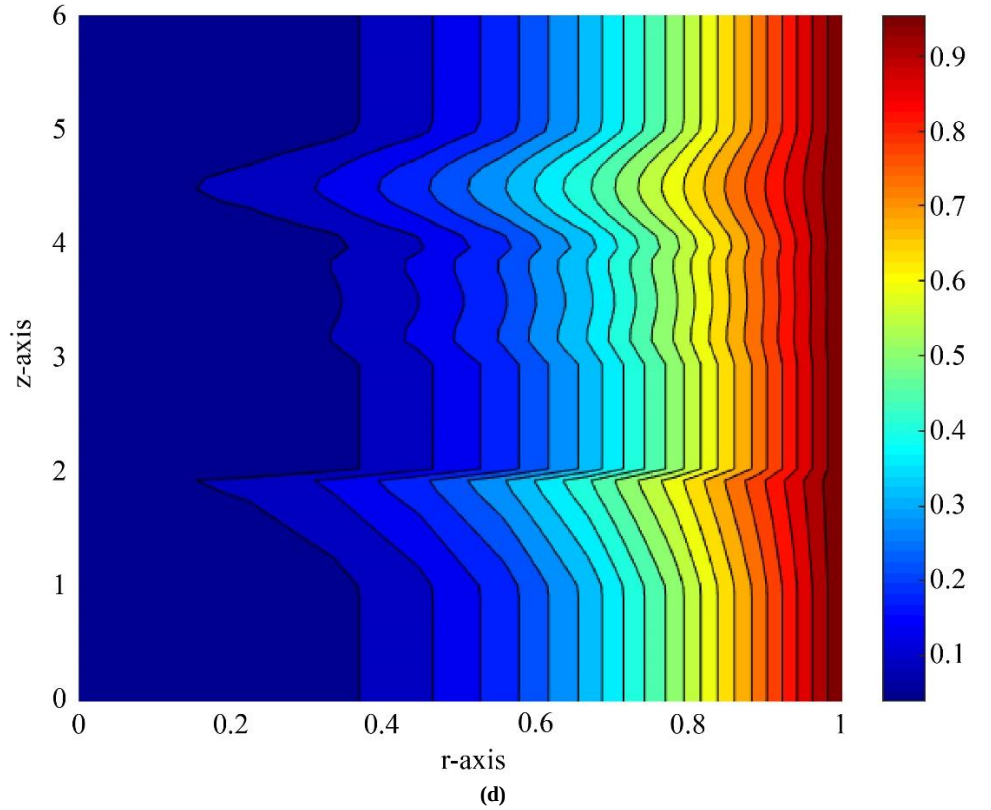
z-axis
r-axis
0
1
2
3
4
5
6
0.2
0.4
0.6
0.8
0.9
0.7
0.5
0.3
0.1

(d)

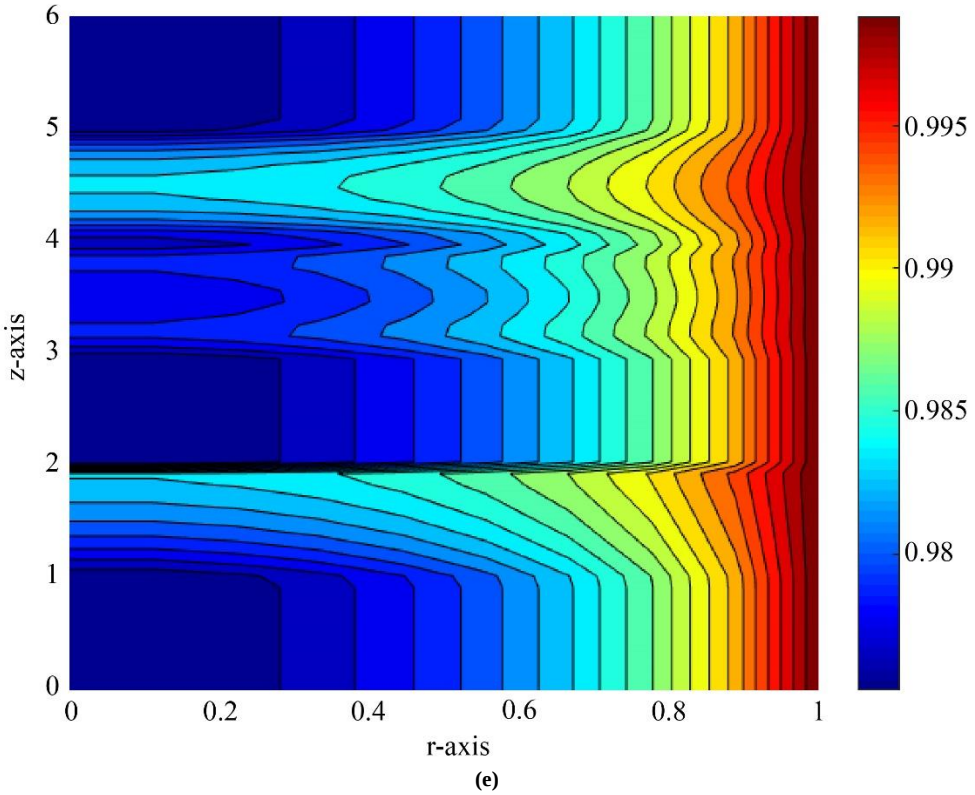

(e)

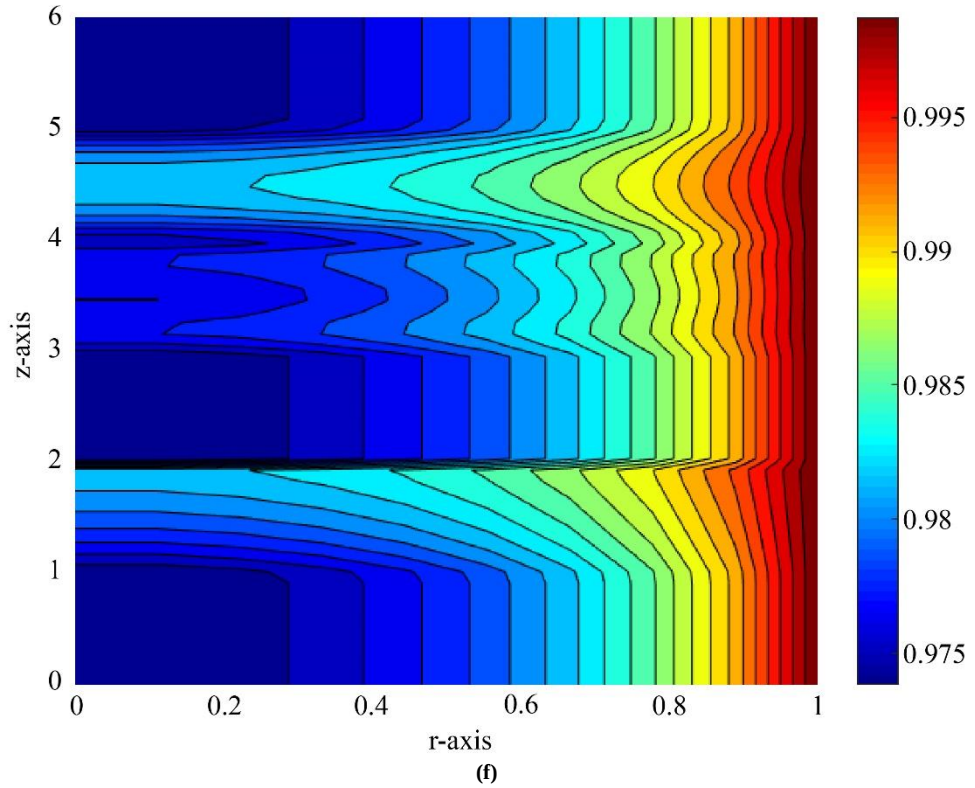

(f)

Fig. 19 Contour plot for three different stenoses in a single artery over time $t = 1$ and (a) velocity contour for pure Blood, (b) velocity contour for hybrid nanofluid ($\phi_{Ag} = \phi_{TiO_2} = 0.04$), (c) temperature contour for pure Blood, (d) temperature contour for hybrid nanofluid ($\phi_{Ag} = \phi_{TiO_2} = 0.04$), (e) concentration contour for pure Blood, (f) concentration contour for hybrid nanofluid ($\phi_{Ag} = \phi_{TiO_2} = 0.04$)

Table 2. Comparison of the concentration profile for the two different values of the activation energy $E_n = 2$ and $E_n = 6$, over time $t = 1$

E_n	z	$r = 0$	$r = 0.5$	$r = 1$
2	z =1.5	0.7083	0.7313	1
	z =3.5	0.6335	0.7406	1
	z =4.5	0.7938	0.8494	1
6	z =1.5	0.7417	0.8257	1
	z =3.5	0.6635	0.7731	1
	z =4.5	0.8315	0.8860	1
% Increment in Concentration	z =1.5	4.71	12.91	0
	z =3.5	4.74	4.39	0
	z =4.5	4.75	4.31	0

Table 3. Grid size comparison of the concentration profile

Mesh size	Concentration
35×8001	0.7131
38×9001	0.7129
41×10001	0.7128
44×11001	0.7128

5. Conclusion

The current hybrid nanofluid model investigates the blood flow behavior with variation of the different flow parameters. The present research introduces a novel mathematical model that investigates blood flow dynamics in an artery featuring three different types of stenosis, namely irregular, overlapping, and elliptical at the distinct locations, addressing a combination of variable thermal conductivity, Reynolds viscosity model, uniform magnetic field, electrical field, and Arrhenius activation energy effects. The suspension of Ag and TiO_2 nanoparticles are incorporated to intensify heat and mass transfer and optimize drug delivery mechanisms with multiple stenoses in a single straight artery. The key findings are as follows:

- The velocity profiles decline with the increments in the values of the Reynolds number (2, 3, and 4) and the magnetic field parameter (1, 1.5, and 2).
- The velocity profiles exhibit an enhancement with the increments in the values of the Darcy number (0.3, 0.5, and 1), electrokinetic parameter (0, 0.4, and 0.8), and the radiation parameter (1, 3, and 5).
- The temperature profiles increase with increases in the values of the Eckert number (0.2, 0.4, and 0.6) and the radiation parameter (1, 3, and 5).
- The temperature profiles decrease with increases in the values of the Prandtl number (7, 14, and 21) and the Reynolds number (2, 3, and 4).
- The concentration profile increases with the increments in the value of the activation energy (2, 4, and 6), and the reverse trend with the increments in the value of the Schmidt number (0.5, 1, and 1.5).
- The WSS increases as the depth of the stenosis (0.1, 0.15, and 0.2) increases, and the Nusselt number decreases as the radiation parameter (1, 3, and 5) increases.
- The Resistance and Sherwood number increase as the magnetic field parameter (2, 3, and 4) and Schmidt number (0.5, 0.8, and 1.1) increase, respectively.
- If the value of the activation energy increases from 2 to 6 then the percentage increment in the concentration profile as 4.71 % increment for the irregular shape of the stenosis, 4.74 % increment for the overlapping shape of the stenosis, and 4.75 % increment for the elliptical shape of the stenosis at the centre of the artery while 12.91 % increment for the irregular shape of the stenosis, 4.39 % increment for the overlapping shape of the stenosis, and 4.31 % increment for the elliptical shape of the stenosis at the 0.5 radius of the artery.

5.1. Limitations and Future Scope

The current work is completed due to the possibility of the hybrid nanofluid blood flow when the behaviour of Blood is non-Newtonian in the artery with three stenosis shapes. There are a few limitations, however, to this research. The Debye-Hückel approximation to linearize Poisson Boltzmann is one of the limitations. In addition, the complications created by the deformation of the wall are presumed to make the wall of the artery rigid. In this study, the approximations of the mild-stenosis are also used. Therefore, these limitations should be mentioned when analyzing the findings and determining the extent of the study. The work may also be extended to further discuss the effect of microorganisms, as this is an area where researchers are doing more research that has not been addressed in this work. The analysis of entropy generation is a significant area that is not studied in the current model.

Conflicts of Interest

The authors declare that there is no conflict of interest regarding the publication of this paper.

Funding Statement

No funding is received from any sources.

Nomenclature

$\tilde{R}_0$	Non-stenotic segment
$\tilde{R}(\tilde{z})$	Stenotic segment
$\tilde{\delta}$	Maximum height for (depth) of the stenosis
$\tilde{z}_s$	Starting point of the overlapping stenotic segment in the artery
$\tilde{z}_l$	Length of the stenotic regions for all shapes (irregular, overlapping, and elliptical)
$\tilde{r}$	Radial coordinate
$\tilde{\theta}$	Circumferential coordinate
$\tilde{z}$	Axial coordinate
ρ_{hnf}	Density of the hybrid nanofluid

μ_{hnf}	Viscosity of the hybrid nanofluid
$S_{\tilde{r}\tilde{r}}$	Normal stress in the radial direction
$S_{\tilde{r}\tilde{z}}$	Shear stress action in $\tilde{z}$ direction on a plane normal to $\tilde{r}$
$S_{\tilde{z}\tilde{z}}$	Stress in the axial direction
$\tilde{p}$	Pressure
$\tilde{t}$	Time
ρ_e	Electrical charge density
$E_{\tilde{z}}$	Electric field in $\tilde{z}$ direction
σ_{hnf}	Electrical conductivity of the hybrid nanofluid
B_0	Applied magnetic field strength
g	Gravitational acceleration
γ_{hnf}	Thermal expansion coefficient
k_p	Permeability of porous medium
$(C_p)_{hnf}$	Specific heat capacity of hybrid nanofluid
$\tilde{q}_{\tilde{r}}$	Radiative heat flux
$\tilde{T}_0$	Reference temperature
$\tilde{T}_w$	Temperature at the wall
D_m	Mass diffusivity
E_n	Activation energy
$k_{\tilde{r}}$	Rate of the chemical reaction
e_0	Electrical charge
n_-	Cation density
n_+	Anion density
$G(\tilde{t})$	body acceleration
z_0	ionic balance
a_g	Amplitude of the body acceleration
w_p	angular frequency
f_b	body force frequency
α	phase angle
A_0	Constant (steady) component of the pressure gradient
A_1	Amplitude of the oscillatory (pulsatile) component,
Sc	Schmidt number
Gr	Thermal Grashof number
Nr	Radiation parameter
Gc	Solutal Grashof number
$\tilde{C}_0$	Reference Concentration
$\tilde{C}_w$	Concentration at the wall
Re	Reynolds number
M	Magnetic field parameter
Da	Darcy number

References

[1] Ayesha Aktar et al., "Biomagnetic Field Effects on Pulsatile Blood Flow with Gold Nanoparticles through Bifurcated Artery with Stenosis and Aneurysm," *Multidiscipline Modeling in Materials and Structures*, vol. 21, no. 5, pp. 1061-1091, 2025. [CrossRef] [Google Scholar] [Publisher Link]

[2] Anjali Chauhan, and Chandi Sasmal, "A Comparative Study of Newtonian and Multi-Mode Viscoelastic Models for Blood Flow in Stenosed Arteries at High Physiologic Reynolds and Womersley Numbers," *International Journal of Engineering Science*, vol. 221, 2026. [CrossRef] [Google Scholar] [Publisher Link]

[3] Azad Hussain, Muhammad Naveel Riaz Dar, and Ahmed Arif, "A Computational Investigation using the non-Newtonian Sisko Model and Finite Element Analysis to Determine Blood Flow Characteristics in Trapezoidal Stenosed Arteries," *International Journal of Modern Physics B*, vol. 39, no. 15, 2025. [CrossRef] [Google Scholar] [Publisher Link]

[4] Azad Hussain, Muhammad Naveel Riaz Dar, and Arosha Iftikhar, "Computational Analysis of Blood Flowing through an Artery with Post Stenotic Dilatation by Implying Sisko Model Parametric Approach," *Scientific Reports*, vol. 16, no. 1, pp. 1-25, 2026. [CrossRef] [Google Scholar] [Publisher Link]

[5] Alex J. Barker et al., "Viscous Energy Loss in the Presence of Abnormal Aortic Flow," *Magnetic Resonance in Medicine*, vol. 72, no. 3, pp. 620-628, 2014. [CrossRef] [Google Scholar] [Publisher Link]

[6] Aditya Singh, and Pramod Kumar Yadav, "ANN-based Computational Framework for EMHD Modulated Ternary Hybrid Nanofluid ($Ag - GO - ZrO_2$/Blood) Flow in a Curved Atherosclerotic Artery," *International Journal of Numerical Methods for Heat and Fluid Flow*, vol. 36, no. 1, pp. 188-227, 2026. [CrossRef] [Google Scholar] [Publisher Link]

[7] A. Zeeshan et al., "Numerical Evaluation of Blood Flow of MHD Non-Newtonian Bingham Fluid with Heat Transfer in a Vertical Artery with Atherosclerosis," *International Journal of Numerical Methods for Heat and Fluid Flow*, vol. 36, no. 1, pp. 275-297, 2026. [CrossRef] [Google Scholar] [Publisher Link]

[8] Bhupendra Kumar Sharma, and Rishu Gandhi, "Entropy-Driven Optimization of Radiative Jeffrey Tetrahybrid Nanofluid Flow through a Stenosed Bifurcated Artery with Hall Effects," *Physics of Fluids*, vol. 35, no. 12, 2023. [CrossRef] [Google Scholar] [Publisher Link]

[9] Bhavya Tripathi, and Bhupendra Kumar Sharma, "Influence of Heat and Mass Transfer on MHD Two-Phase Blood Flow with Radiation," *AIP Conference Proceedings*, vol. 1975, no. 1, 2018. [CrossRef] [Google Scholar] [Publisher Link]

[10] Chandrakanta Parida, Ganeswar Mahanta, and Sachin Shaw, "Nonlinear Hemodynamics Modeling of Fractional Jeffery Ternary Hybrid Nanofluid Flow in Multi-Stenosed Arteries with ANN-based Simulation," *Nonlinear Dynamics*, vol. 113, no. 25, pp. 34873-34904, 2025. [CrossRef] [Google Scholar] [Publisher Link]

[11] D.S. Sankar, and K. Hemalatha, "A Non-Newtonian Fluid Flow Model for Blood Flow through a Catheterized Artery Steady Flow," *Applied Mathematical Modelling*, vol. 31, no. 9, pp. 1847-1864, 2007. [CrossRef] [Google Scholar] [Publisher Link]

[12] Fatima Shafiq Hira et al., "Advanced Computational Modeling of Darcy-Forchheimer Effects and Nanoparticle-Enhanced Blood Flow in Stenosed Arteries," *Engineering Applications of Artificial Intelligence*, vol.152, 2025. [CrossRef] [Google Scholar] [Publisher Link]

[13] Gordon D. Smith, *Numerical Solution of Partial Differential Equations: Finite Difference Methods*, 3rd ed., Oxford University Press, 1985. [Google Scholar] [Publisher Link]

[14] Haris Alam Zuberi et al., "Numerical Simulation of Blood Flow Dynamics in a Stenosed Artery Enhanced by Copper and Alumina Nanoparticles," *Computer Modeling in Engineering and Sciences*, vol. 142, no. 2, pp. 1839-1864, 2025. [CrossRef] [Google Scholar] [Publisher Link]

[15] Issa El Glili et al., "Numerical Simulation of Unsteady Blood based Carreau Nanofluid Flow in an Inclined Porous Saturated Artery having Overlapping Stenosis with Electro-osmosis," *Numerical Heat Transfer, Part A: Applications*, vol. 86, no. 21, pp. 7749-7779, 2024. [CrossRef] [Google Scholar] [Publisher Link]

[16] Jamil Abbas Haider et al., "Multifaceted Simulation: Finite volume and Finite Element Modeling of Blood Flow in Multiple Stenosed Arteries," *Modern Physics Letters B*, vol. 39, no. 3, 2025. [CrossRef] [Google Scholar] [Publisher Link]

[17] Jayati Tripathi, B. Vasu, and O. Anwar Bég, "Computational Simulations of Hybrid Mediated Nano-Hemodynamics (Ag-Au/Blood) through an Irregular Symmetric Stenosis," *Computers in Biology and Medicine*, vol. 130, pp. 1-42, 2021. [CrossRef] [Google Scholar] [Publisher Link]

[18] Jayati Tripathi et al., "Unsteady Hybrid Nanoparticle-Mediated Magneto-Hemodynamics and Heat Transfer through an Overlapped Stenotic Artery: Biomedical Drug Delivery Simulation," *Proceedings of the Institution of Mechanical Engineers, Part H: Journal of Engineering in Medicine*, vol. 235, no. 10, pp. 1175-1196, 2021. [CrossRef] [Google Scholar] [Publisher Link]

[19] Jayati Tripathi et al., "Computational Simulation of Rheological Blood Flow Containing Hybrid Nanoparticles in an Inclined Catheterized Artery with Stenotic, Aneurysmal and Slip Effects," *Computers in Biology and Medicine*, vol. 139, 2021. [CrossRef] [Google Scholar] [Publisher Link]

[20] Stefan Lecheler, Computational Fluid Dynamics: Getting Started Quickly With ANSYS CFX 18 Through Simple Examples, 1st ed., Springer Wiesbaden, 2022. [Publisher Link]

[21] K.N. Asha, and Neetu Srivastava, "Analysis of Blood Flow Features in the Curved Artery in the Presence of Differently Shaped Hybrid Nanoparticles," *Partial Differential Equations in Applied Mathematics*, vol. 13, pp. 1-7, 2025. [CrossRef] [Google Scholar] [Publisher Link]

[22] Kannigah Thirunananasambantham et al., "Computational Analysis of Hybrid GPL Blood Nanofluid Flow Over Various Stenosed Arteries in the Presence of a Magnetic Field," *Alexandria Engineering Journal*, vol. 129, pp. 598-611, 2025. [CrossRef] [Google Scholar] [Publisher Link]

[23] Lilibeth P. Coronel, Rey Y. Capangpangan, and Ruji P. Medina, "Engineered Nanoparticles Cytotoxicity Prediction using an Enhanced Convolutional Neural Network," *International Journal of Engineering Trends and Technology*, vol. 73, no. 6, pp. 309-317, 2025. [CrossRef] [Google Scholar] [Publisher Link]

[24] Mohammadamin Bagherkhani, Saeed Dinarvand, and Mohammad Vahabi, "Modeling of Blood Flow in an Irregular Multi-stenosed Vessel in Presence of Iron Oxide and Gold Nanoparticles," *BioNanoScience*, vol. 15, no. 1, 2025. [CrossRef] [Google Scholar] [Publisher Link]

[25] Mallinath Dhange et al., "Hemodynamic Characteristics of Blood Flow in an Inclined Overlapped Stenosed Arterial Section," *Partial Differential Equations in Applied Mathematics*, vol. 11, pp. 1-7, 2024. [CrossRef] [Google Scholar] [Publisher Link]

[26] M. Dhange et al., "Hemodynamic Properties of Blood Flow in an Angled Overlying Stenosed Blood Vessel via Force Field and Gold Nanoparticle Suspension," *Scientific African*, vol. 28, pp. 1-13, 2025. [CrossRef] [Google Scholar] [Publisher Link]

[27] M.H. Shah et al., "A Caputo Time-Fractional Derivative Approach to Pulsatile Non-Newtonian Sutterby Blood Fluid Flow through a Vertical Stenotic Artery under MHD Influence," *Journal of Computational Applied Mechanics*, vol. 57, no. 1, pp. 63-83, 2026. [Google Scholar]

[28] N. Ameer Ahammad, and Abdulwahab Ali Mohammed Al Talea, "MHD Rotating Flow Over a Semi-Infinite Vertical Moving Plate with Oscillatory Effects," *International Journal of Engineering Trends and Technology*, vol. 69, no. 10, pp. 161-167, 2021. [CrossRef] [Publisher Link]

[29] Noreen Sher Akbar, "Biomathematical Study of Sutterby Fluid Model for Blood Flow in Stenosed Arteries," *International Journal of Biomathematics*, vol. 8, no. 6, 2015. [Google Scholar] [Publisher Link]

[30] Pramod Kumar Yadav, and Aditya Singh, "Biomedical Simulations of Electroosmotic Non-Newtonian Hybrid Nanofluid (Blood) with Hematocrit Viscosity through a Porous Overlapping Irregular Stenosed Artery," *Computers in Biology and Medicine*, vol. 196, 2025. [CrossRef] [Google Scholar] [Publisher Link]

[31] Pooriya Majidi Zar, Zahra Poolaei Moziraji, and Ali Ahmadi Azar, "Mathematical Modeling of Blood Flow with Copper and Graphene Nanoparticles in Inclined Stenotic Arteries," *Scientific Reports*, vol. 15, no. 1, pp. 1-26, 2025. [CrossRef] [Google Scholar] [Publisher Link]

[32] Rahmat Ellahi, Mohsin Raza, and Kambiz Vafai, "Series Solutions of Non-Newtonian Nanofluids with Reynolds' Model and Vogel's Model by Means of the Homotopy Analysis Method," *Mathematical and Computer Modelling*, vol. 55, no. 7-8, pp. 1876-1891, 2012. [CrossRef] [Google Scholar] [Publisher Link]

[33] Rishu Gandhi et al., "Modeling and Analysis of Magnetic Hybrid Nanoparticle ($Au - Al_2O_3$/blood) based Drug Delivery through a Bell-Shaped Occluded Artery with Joule Heating, Viscous Dissipation and Variable Viscosity Effects," *Proceedings of the Institution of Mechanical Engineers, Part E: Journal of Process Mechanical Engineering*, vol. 236, no. 5, pp. 2024-2043, 2022. [CrossRef] [Google Scholar] [Publisher Link]

[34] Rishu Gandhi et al., "Entropy Generation and Shape Effects Analysis of Hybrid Nanoparticles ($Cu - Al_2O_3$/blood) Mediated Blood Flow through a Time-Variant Multi-Stenotic Artery," *International Journal of Thermofluids*, vol. 18, pp. 1-13, 2023. [CrossRef] [Google Scholar] [Publisher Link]

[35] Ramakrishna Manchi, and R. Ponalagusamy, "Pulsatile Flow of EMHD Micropolar Hybrid Nanofluid in a Porous Bifurcated Artery with an Overlapping Stenosis in the Presence of Body Acceleration and Joule Heating," *Brazilian Journal of Physics*, vol. 52, no. 2, 2022. [CrossRef] [Google Scholar] [Publisher Link]

[36] Sara I. Abdelsalam, and M.M. Bhatti, "Synergistic Progression of Nanoparticle Dynamics in Stenosed Arteries," *Qualitative Theory of Dynamical Systems*, vol. 24, no. 1, 2025. [CrossRef] [Google Scholar] [Publisher Link]

[37] Saiful Islam et al., "Electroosmotic Flow in Ternary ($TiO_2 - SiO_2 - Al_2O_3$) Blood-based Sutterby Nanomaterials with Bio-Active Mixers," *International Journal of Thermofluids*, vol. 18, pp. 1-15, 2023. [CrossRef] [Google Scholar] [Publisher Link]

[38] Syed M. Hussain, "Irreversibility Analysis of Time-Dependent Magnetically Driven Flow of Sutterby Hybrid Nanofluid: A Thermal Mathematical Model," *Waves in Random and Complex Media*, vol. 35, no. 4, pp. 7628-7660, 2025. [CrossRef] [Google Scholar] [Publisher Link]

[39] Suneetha Sangapatnam, "Casson Flow of Blood Containing Au and Ta Nanoparticles Over a Stenotic Artery," *East European Journal of Physics*, no. 1, pp. 309-317, 2025. [CrossRef] [Google Scholar] [Publisher Link]

[40] Souhail Souai et al., "Assessment of Heat and Mass Transfer in a Porous N-Shaped Heat Exchanger using Hybrid Nanofluid under Cross-Diffusion and Magnetic Effects," *European Journal of Mechanics-B/Fluids*, vol. 114, 2025. [CrossRef] [Google Scholar] [Publisher Link]

[41] Suneetha Sangapatnam, and Ramasekhar Gunisetty, "Computational Role of Blood-based Casson Fluid Flow through a Stenotic Artery: An Application to Cardiovascular Issues," *Thermal Science*, vol. 29, no. 2, pp. 3267-3277, 2025. [CrossRef] [Google Scholar] [Publisher Link]

[42] Taimoor Salahuddin et al., "Blood Flow Study in Stenotic Arteries through Porous Medium with Heat Generation," *International Communications in Heat and Mass Transfer*, vol. 164, 2025. [CrossRef] [Google Scholar] [Publisher Link]

[43] Yasir Ul Umair Bin Turabi et al., "FEM Simulation to Predict Thermal Enhancement Mechanism in Nanoparticles Laden blood Flow through an Inflamed Stenosis Artery with Magnetohydrodynamics Effect," *Multiscale and Multidisciplinary Modeling, Experiments and Design*, vol. 8, no. 5, 2025. [CrossRef] [Google Scholar] [Publisher Link]